



**HAL**  
open science

# The anomalous polymict ordinary chondrite breccia of Elmshorn ( H3 -6)-Late reaccretion after collision between two ordinary chondrite parent bodies, complete disruption, and mixing possibly about 2.8 Gyr ago

Addi Bischoff, Markus Patzek, Romain Alosius, Jean-Alix Barrat, Jasper Berndt, Henner Busemann, Detlev Degering, Tommaso Di Rocco, Mattias Ek, Jérôme Gattacceca, et al.

## ► To cite this version:

Addi Bischoff, Markus Patzek, Romain Alosius, Jean-Alix Barrat, Jasper Berndt, et al.. The anomalous polymict ordinary chondrite breccia of Elmshorn ( H3 -6)-Late reaccretion after collision between two ordinary chondrite parent bodies, complete disruption, and mixing possibly about 2.8 Gyr ago. *Meteoritics and Planetary Science*, 2024, 10.1111/maps.14193 . hal-04612235

**HAL Id: hal-04612235**

**<https://hal.univ-brest.fr/hal-04612235>**

Submitted on 14 Jun 2024











**HAL** is a multi-disciplinary open access archive for the deposit and dissemination of scientific research documents, whether they are published or not. The documents may come from teaching and research institutions in France or abroad, or from public or private research centers.

L'archive ouverte pluridisciplinaire **HAL**, est destinée au dépôt et à la diffusion de documents scientifiques de niveau recherche, publiés ou non, émanant des établissements d'enseignement et de recherche français ou étrangers, des laboratoires publics ou privés.



Distributed under a Creative Commons Attribution 4.0 International License

# The anomalous polymict ordinary chondrite breccia of Elmshorn (H3-6)—Late reaccretion after collision between two ordinary chondrite parent bodies, complete disruption, and mixing possibly about 2.8 Gyr ago

Addi BISCHOFF <sup>1,\*</sup>, Markus PATZEK <sup>1</sup>, Romain M. L. ALOSIOUS <sup>2</sup>, Jean-Alix BARRAT<sup>3,4</sup>, Jasper BERNDT<sup>5</sup>, Henner BUSEMANN <sup>2</sup>, Detlev DEGERING<sup>6</sup>, Tommaso DI ROCCO<sup>7</sup>, Mattias EK <sup>2</sup>, Jérôme GATTACCECA <sup>8</sup>, Jose R. A. GODINHO<sup>9</sup>, Dieter HEINLEIN<sup>10</sup>, Daniela KRIETSCH <sup>2</sup>, Colin MADEN <sup>2</sup>, Oscar MARCHHART<sup>11</sup>, Martin MARTSCHINI<sup>11</sup>, Silke MERCHEL<sup>11</sup>, Andreas PACK<sup>7</sup>, Stefan PETERS<sup>12</sup>, Miriam RÜFENACHT <sup>2</sup>, Jochen SCHLÜTER<sup>12</sup>, Maria SCHÖNBÄCHLER <sup>2</sup>, Aleksandra STOJIC<sup>1</sup>, Jakob STORZ<sup>1</sup>, Wolfgang TILLMANN<sup>13</sup>, Alexander WIESER<sup>11</sup>, Karl WIMMER<sup>14</sup>, and Reiner ZIELKE<sup>13</sup>

<sup>1</sup>Institut für Planetologie, University of Münster, Münster, Germany

<sup>2</sup>Institute of Geochemistry and Petrology, ETH Zürich, Zurich, Switzerland

<sup>3</sup>Univ Brest, CNRS, Ifremer, IRD, LEMAR, Institut Universitaire Européen de la Mer (IUEM), Place Nicolas Copernic, Plouzané, France

<sup>4</sup>Institut Universitaire de France, Paris, France

<sup>5</sup>Institut für Mineralogie, University of Münster, Münster, Germany

<sup>6</sup>VKTA—Strahlenschutz, Analytik & Entsorgung Rossendorf e. V., Dresden, Germany

<sup>7</sup>Geowissenschaftliches Zentrum, Universität Göttingen, Göttingen, Germany

<sup>8</sup>CNRS, Aix Marseille Univ, IRD, INRAE, CEREGE, Aix-en-Provence, France

<sup>9</sup>Helmholtz-Zentrum Dresden-Rossendorf, Helmholtz Institute Freiberg for Resource Technology, Freiberg, Germany

<sup>10</sup>German Fireball Network, Augsburg, Germany

<sup>11</sup>Faculty of Physics, Isotope Physics, University of Vienna, Vienna, Austria

<sup>12</sup>Museum der Natur Hamburg—Mineralogie, LIB, Hamburg, Germany

<sup>13</sup>RIF Institut für Forschung und Transfer e.V., Dortmund, Germany

<sup>14</sup>Salvatorgasse 12, Nördlingen, Germany

## \*Correspondence

Addi Bischoff, Institut für Planetologie, University of Münster, Wilhelm-Klemm-Str. 10, Münster D-48149, Germany.

Email: [bischoa@uni-muenster.de](mailto:bischoa@uni-muenster.de)

(Received 18 December 2023; revision accepted 06 May 2024)

**Abstract**—Elmshorn fell April 25, 2023, about 30 km northwest of the city of Hamburg (Germany). Shortly after the fall, 21 pieces were recovered totaling a mass of 4277 g. Elmshorn is a polymict and anomalous H3-6 chondritic, fragmental breccia. The rock is a mixture of typical H chondrite lithologies and clasts of intermediate H/L (or L, based on magnetic properties) chondrite origin. In some of the 21 pieces, the H chondrite lithologies dominate, while in others the H/L (or L) chondrite components are prevalent. The H/L chondrite assignment of these components is based on the mean composition of their olivines in equilibrated type 4 fragments ( $\sim\text{Fa}_{21-22}$ ). The physical properties like density ( $3.34 \text{ g cm}^{-3}$ ) and magnetic susceptibility ( $\log\chi < 5.0$ , with  $\chi$  in  $10^{-9} \text{ m}^3 \text{ kg}^{-1}$ ) are typical for L chondrites, which is inconsistent with the oxygen isotope compositions: all eight O isotope analyses from two different fragments clearly fall into the H chondrite field. Thus, the fragments found in the strewn field vary in mineralogy, mineral chemistry, and physical properties but not in O isotope characteristics. The sample most intensively studied belongs to the stones dominated by H chondrite lithologies. The chemical composition and nucleosynthetic Cr and Ti isotope

data are typical for ordinary chondrites. The noble gases in Elmshorn represent a mixture between cosmogenic, radiogenic, and primordially trapped noble gases, while a solar wind component can be excluded. Because the chondritic rock of Elmshorn contains (a) H chondrite parent body interior materials (of types 5 and 6), (b) chondrite parent body near-surface materials (of types 3 and 4), (c) fragments of an H/L chondrite (dominant in many stones), (d) shock-darkened fragments, and (e) clasts of various types of impact melts but no solar wind-implanted noble gases, the different components cannot have been part of a parent body regolith. The most straightforward explanation is that the fragmental breccia of Elmshorn represents a reaccreted rock after a catastrophic collision between an H chondrite parent body and another body with H/L (or L) chondrite characteristics but with deviating O isotope values (i.e. that of H chondrites), complete disruption of the bodies, mixing, and reassembly. This is the only straightforward way that the implantation of solar wind gases could have been avoided in this kind of complex breccia. The gas retention ages of about 2.8 Gyr possibly indicate the closure time after the catastrophic collision between H and H/L (or L) chondrite parent bodies, while the cosmic ray exposure age for Elmshorn, which had a preatmospheric radius of 25–40 cm, is  $\sim 17$ –20 Myr.

## INTRODUCTION

Due to catastrophic collisions between asteroids and smaller impacts on solar system bodies, different processes can lead to the modification of meteorite parent bodies, the formation of new bodies, and the emergence of new rock types. These processes include, for example, accretion, excavation of material, thermal metamorphism, reduction processes, melting, mixing of different material, reaccretion, and relithification (e.g., Bischoff et al., 2006, 2018; Keil, 1982; Rubin & Turrin, 2023). All these processes can be repeated many times and may lead to complex meteorite breccias that contain a large variety of fragments and lithologies, which is also the case for Elmshorn.

Elmshorn fell April 25, 2023, about 30 km northwest of the city of Hamburg (Germany). The daytime fireball at 12:14:24 UT was recorded for a duration of 3 s by two meteor cameras of the Allsky7 network and observed by eyewitnesses in northern Germany and the Netherlands (<https://fma.imo.net>). Exactly 117 s after the bolide appeared, a 3731 g stony meteorite struck an Elmshorn garden on Irena-Sendler-Strasse and penetrated 30–40 cm deep into the ground (sample E01; Table S1). The impact was acoustically recorded by a nearby surveillance camera. Shortly thereafter, smaller pieces hit the roofs of two Elmshorn homes, damaging several roof tiles. Intensive search activities led to the discovery of complete meteorite pieces or their fragments at another 18 locations in the northern city area of Elmshorn. Details about the recovered 21 pieces are given in Table S1. Besides the main mass mentioned before, one of the first recognized pieces of 233.5 g (E02) crashed into the roof of a house on the street Iltisweg. Another large piece of about 156 g (E03) broke into many pieces after strongly impacting the roof

of a house on Gärtnerstrasse. Some examples are shown in Figure 1. The finding that these are fresh meteorite samples is supported by short-lived cosmogenic radionuclide detection by gamma spectrometry in E01 and E02. The presence of short-lived cosmogenic radionuclides with half-lives as short as 5.6 days proves that the fallen and recovered object was recently exposed to cosmic rays in space, linking it clearly to the bolide event. Elmshorn has been classified as a polymict H3-6 chondritic breccia (The Meteoritical Bulletin, 2023). The first rock studied in detail (E03) mainly contains H chondrite lithologies but also abundant clasts of intermediate H/L (or L) chondrite heritage. A second individual sample (E07) from the strewn field studied for comparison shows abundant fragments of H/L (or L) chondrite origin.

In central Europe, 11 meteorite falls (including Elmshorn) have been recovered in an area less than 500 km in radius in the last 10 years. Ten falls were found to be ordinary chondrites (OCs), while only one (Flensburg) represents a small extraordinary C1 chondrite of 24 g (The Meteoritical Bulletin, 2023). Remarkably, the two most scientifically interesting samples, namely Flensburg and Elmshorn, fell only 110 km apart within a period of only 4 years.

## SAMPLES, ANALYTICAL PROCEDURES, MODEL CONSIDERATIONS, AND THE FIND LOCATIONS OF THE ELSHORN METEORITE

### Studied Samples

In the days following the meteorite fall, 21 individual meteorite samples were recovered within a strewn field of about  $1.5 \times 2.5$  km<sup>2</sup> (Figure 2). Images of typical locations of the find area are given in Figure 3.

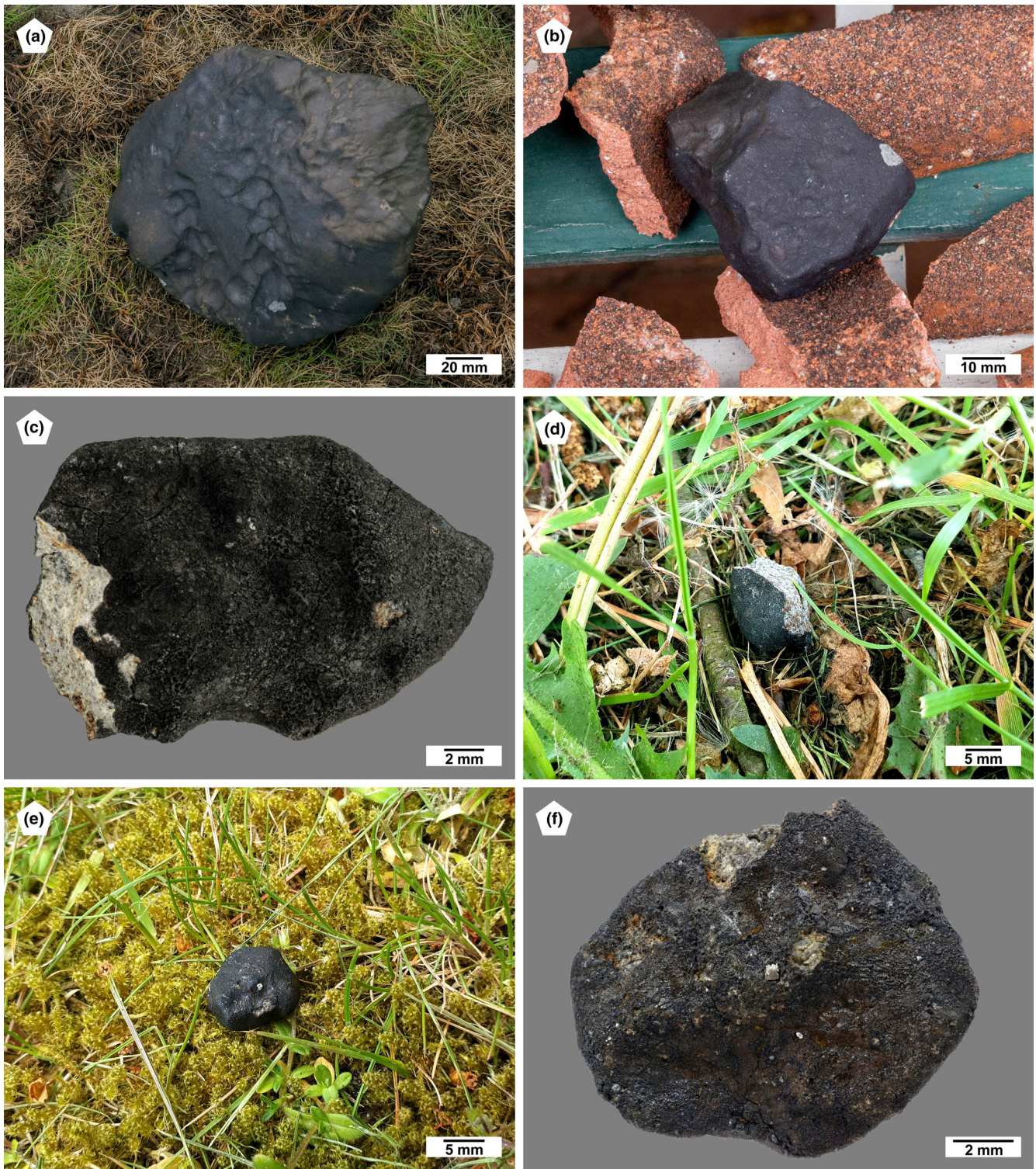


FIGURE 1. Images of six (of the total 21) Elmshorn stony meteorites found between April 25 and May 29, 2023. (a) The E01 (Table S1), weighing 3731 g, struck a garden and made a hole in the lawn 30–40 cm deep. (b) An individual piece of Elmshorn, E02, weighing 233.5 g, hit the roof of a house, was recovered within a few minutes, and felt hand-warm, as reported by the finder. (c) Piece E11, at 7.98 g, has a dull black fusion crust and a broken edge. (d) This broken meteorite fragment, E15, weighing 3.40 g, was discovered on the grassy side of a road. (e) This complete chondrite specimen E18, weighing 2.43 g, was found lying in the moss at the Elmshorn cemetery. (f) The smallest recovered complete piece, E21, of 1.09 g, hit the terrace of a house in Elmshorn; the fusion-crust surface of the meteorite shows its flight orientation and a metal inclusion.



FIGURE 2. Locations and distribution of the meteorites: From April 25 to May 29, 2023, stony meteorites were found at 21 different locations in the northern part of the city of Elmshorn: The 3731 g main mass (E01) is marked by a magenta dot (upper left). Red dots represent two specimens in the range of 100–1000 g, and orange dots represent three pieces weighing 10–100 g. The 15 small meteorite finds (1–10 g) are marked in yellow and were mostly found in an area northeast of the railway tracks. The two samples studied in more detail are marked by arrows. Samples E01 and E02 were used for nondestructive gamma spectrometry. Source of base map: Google Earth.

The first studied fragment of Elmshorn was recovered April 26, 2023 (1 day after the fall). From the scattered (in total 156 g; E03) piece, a sample of 20.5 g was used for classification procedures. We crushed about 0.6 g to reveal a coarse-grained, relatively homogeneous powder. This powder still contained large (>0.5 mm) particles due to many large metal–sulfide associations present in the samples that are difficult to destroy. Four thin sections of the rock (fragment E03; PL23028, PL23029, PL23030, PL23031), with an area of  $\sim 3.5 \text{ cm}^2$  each, were available for optical and electron microscopic studies. For comparison, a second sample from E07 was studied in a polished section (PL23047) of  $\sim 0.75 \text{ cm}^2$ , and small pieces of E07 were used for additional analyses of oxygen isotopes and magnetic susceptibility (MS). This sample was found about 1 month after the fall on May 27, 2023.

## Analytical Procedures and Model Considerations

### Mineralogical Studies

At the Institut für Planetologie (University of Münster), an Axiophot polarizing microscope (Fa. ZEISS) was used for optical microscopy in transmitted and reflected light. At the same institution, a JEOL 6610-LV electron microscope (SEM) was used to study the brecciated texture of the Elmshorn samples and to identify

the different mineral phases. Some chemical data were obtained using the INCA analytical program provided by Oxford Instruments for energy-dispersive spectrometry.

Most quantitative mineral analyses were obtained with a JEOL JXA 8530F electron microprobe at the Institut für Mineralogie (University of Münster), which was operated at 15 kV and a probe current of 15 nA. Synthetic and natural standards were used for wavelength-dispersive spectrometry. As standards for mineral analyses, we used jadeite (Na), San Carlos olivine (Mg), kyanite (Al), hypersthene (Si), sanidine (K), chromium oxide (Cr), diopside (Ca), rhodonite (Mn), rutile (Ti), fayalite (Fe), apatite (P), celestine (S), Co metal (Co), and nickel oxide (Ni). We have checked the peak situation and found no overlap of the Fe- $K_{\beta}$  peak on the Co- $K_{\alpha}$  peak.

### Bulk Chemical Analysis

From the crushed and homogenized material from fragment E03, about 180 mg was used for bulk chemical analyses at the University of Brest. The chemical bulk composition of Elmshorn was obtained using inductively coupled plasma atomic emission spectrometry (ICP-AES; for Fe, Mn, Mg, Na, Cr, Co, and Ni) and inductively coupled plasma sector field mass spectrometry (ICP-SFMS). The concentration reproducibility is generally



FIGURE 3. (a) Small forest in the north of Elmshorn on Kaltenhof street, close to the place where sample E04 (Table S1) was found; (b) area in the northwestern part of the strewn field close to the find location of the 3.7 kg piece (E01); (c) grain field west of the Irena-Sendler city area of Elmshorn; (d) view into the street Iltisweg, where the 233.5 g (E02) sample crashed onto a roof; (e) north of the railway tracks, samples were searched for by a drone; (f) a grassland east of Iltisweg and north of the railway tracks after the grass was cut in early June.

greater than 5%. Further details concerning the analytical method are reported by Barrat et al. (2012, 2016).

### Oxygen Isotope Analyses

Measuring the oxygen isotope composition is an important tool for classifying meteorites (e.g., Clayton et al., 1976). For Elmshorn, the compositions of eight chips (each weighing between 2.0 and 2.3 mg) from two recovered pieces (E03 and E07) were obtained by means of laser fluorination in combination with a gas source mass spectrometer. The analytical techniques are given in detail in Pack et al. (2016) and Peters et al. (2020; also, compare Herwartz et al. 2014; Pack & Herwartz, 2014; Pack et al., 2017). The  $\delta^{17}\text{O}$  and  $\delta^{18}\text{O}$  values are reported on the VSMOW (Vienna Standard Mean Ocean Water) scale, and the  $\Delta^{17}\text{O}$  is defined here as:

$$\Delta^{17}\text{O} = 1000 \ln\left(\frac{\delta^{17}\text{O}}{1000} + 1\right) - 0.528 \\ \times 1000 \ln\left(\frac{\delta^{18}\text{O}}{1000} + 1\right).$$

To anchor  $\delta^{17}\text{O}$  on the VSMOW scale, we used a  $\Delta^{17}\text{O}$  value for San Carlos olivine of  $-0.052\text{‰}$  (average value of Pack et al., 2016; Sharp et al., 2016; Wostbrock et al., 2020). In this study, the estimated measurement uncertainties are  $\pm 0.1\text{‰}$  for  $\delta^{18}\text{O}$  and  $\pm 0.01\text{‰}$  for  $\Delta^{17}\text{O}$ , and these data are based on replicate analyses of the San Carlos olivine standard (1 SD).

### Titanium and Chromium Isotope Analysis

For nucleosynthetic Ti and Cr isotope analyses of the Elmshorn meteorite, 28.66 mg of powdered material from E03 was used. The powder was dissolved in octagonal Savillex<sup>®</sup> vials following the procedure in Bischoff, Barrat, et al. (2019). Titanium was separated and purified in a three-step anion exchange chromatography procedure as described in Williams et al. (2021). Chromium was separated from the matrix fraction of the first Ti ion exchange procedure using a two-step cation exchange procedure described in Bischoff, Barrat, et al. (2019). The blank of the full chemical procedure was 1.7 ng Ti and 20 ng Cr. This corresponds to a blank contribution of maximum 0.014% for Ti and 0.027% for Cr.

The Ti isotope analyses were performed on a Thermo Scientific Neptune Plus multi-collector inductively coupled plasma mass spectrometer (MC-ICPMS) at ETH Zurich, following the description in Rufenacht et al. (2023). The measurements were done in medium mass resolution (MR) with a mass resolving power  $R \sim 6500$  ( $R = m/[m_{0.95} - m_{0.05}]$ ). One single measurement consumed  $\sim 0.5 \mu\text{g}$  Ti and achieved a signal of  $\sim 40$  V over a  $10^{11}$  Ohm resistor on  $^{48}\text{Ti}$ . The isotope data were

corrected for instrumental mass bias by normalizing to the  $^{49}\text{Ti}/^{47}\text{Ti}$  ratio of 0.749766 (Niederer et al., 1985), using the exponential law. The data are reported relative to an in-house Alfa Aesar Ti wire standard in the  $\epsilon$  notation and applying the sample-standard bracketing method:

$$\epsilon^i\text{Ti} = \left( \frac{i/47\text{Ti}_{\text{sample}}}{i/47\text{Ti}_{\text{standard}}} - 1 \right) \times 10^4,$$

where  $i$  stands for the isotope masses  $^{46}\text{Ti}$ ,  $^{48}\text{Ti}$ , and  $^{50}\text{Ti}$ . The isotope data were collected on four different days and include 10 repeat measurement for Elmshorn. Parallel to the Elmshorn meteorite, the terrestrial rock standard BHVO-2 and the OC Forest Vale (H4) were measured to assess the accuracy and reproducibility of the measurements.

Chromium isotope analyses were also performed at ETH Zurich on a Thermo Scientific Neptune Plus MC-ICP-MS following the procedure outlined in Rufenacht et al. (2023). All measurements were performed in medium resolution with a typical resolving power of  $R \sim 6500$ . Approximately  $0.5 \mu\text{g}$  Cr was consumed for a single measurement which corresponded to a signal of  $\sim 110$  V on  $^{52}\text{Cr}$ . Instrumental mass fractionation was corrected relative to  $^{50}\text{Cr}/^{52}\text{Cr} = 0.051859$  (Shields et al., 1966) using the exponential law. Sample measurements were bracketed with measurements of the NIST SRM 979 standard and Cr isotope data are reported in  $\epsilon$  notation relative to these standards:

$$\epsilon^i\text{Cr} = \left( \frac{i/52\text{Cr}_{\text{sample}}}{i/52\text{Cr}_{\text{standard}}} - 1 \right) \times 10^4,$$

where  $i$  stands for the isotope masses  $^{53}\text{Cr}$  and  $^{54}\text{Cr}$ . Elmshorn was measured six times in three different analytical sessions. In addition to Elmshorn, the terrestrial rock standard DTS-2 was measured in all sessions to monitor the accuracy and reproducibility of the measurements.

### Noble Gas Mass Spectrometry

All stable noble gas isotopes (He-Xe) were measured on two aliquots of  $15.307 \pm 0.023$  mg (“Elmshorn 1”) and  $15.090 \pm 0.026$  mg (“Elmshorn 2”) from stone E03 (Table S1). The aliquots were wrapped in aluminum foil and heated to  $110^\circ\text{C}$  for several days in a sample chamber to degas adsorbed atmospheric gases. The measurements were performed on the in-house built noble gas mass spectrometer called Albatros at ETH Zürich following procedures further described in Riebe et al. (2017). The noble gases were extracted in a Mo crucible by heating the samples to  $\sim 1700^\circ\text{C}$  for  $\sim 25$  min. Blank corrections

for Elmsborn 1 and 2 are <0.4% of the He and Ne isotope signals, <4.9% for Ar, and <1.7% of the signals for all Kr and Xe isotopes.

### *Instrumental Accelerator Mass Spectrometry for Cosmogenic $^{26}\text{Al}$ and $^{41}\text{Ca}$*

Accelerator mass spectrometry (AMS) is the method of choice for the detection of long-lived cosmogenic radionuclides such as  $^{26}\text{Al}$  and  $^{41}\text{Ca}$  ( $t_{1/2} = 0.705$  and  $0.104$  Myr, respectively; Norris et al., 1983; Paul et al., 1991). Recently, a worldwide unique development at the Vienna Environmental Research Accelerator (VERA), an ion-laser interaction mass spectrometry (ILIAMS) system allows the isobar suppression by up to 14 orders of magnitude (Martschini et al., 2022). Hence, ILIAMS-assisted AMS, so-called instrumental AMS (IAMS), enables now the direct detection of  $^{26}\text{Al}/^{27}\text{Al}$  ( $\sim 10^{-10}$ ) and  $^{41}\text{Ca}/^{40}\text{Ca}$  ( $\sim 10^{-12}$ ) in crushed Elmsborn containing intrinsic  $\sim 1\%$  Al and Ca. Isobars from the natively abundant elements (12.6% Mg, 1% K) do not cause any analysis problem making radiochemical separation redundant. IAMS was performed on an additionally crushed aliquot ( $\sim 75$  mg) of the 0.6 g powder of E03. For  $\text{AlO}^-$  extraction and  $^{26}\text{Al}/^{27}\text{Al}$  measurements (Lachner et al., 2021), a small portion of the fine-grained powder was pressed without any metal binder in Cu cathodes. For  $^{41}\text{Ca}/^{40}\text{Ca}$   $\sim 1$  mg powder was mixed with  $\sim 9$  mg of  $\text{PbF}_2$  to increase  $\text{CaF}_3^-$  extraction from the Cs ion sputter source and finally also pressed in Cu cathodes. In-house standards “Dhurmsala” ( $^{26}\text{Al}/^{27}\text{Al} = [1.287 \pm 0.0341] \times 10^{-10}$ ) and SMD-Ca-12, traceable to primary standards (Rugel et al., 2016), have been used for normalization. IAMS data total uncertainties include counting statistics and scatter for each sample, the variability of the measurements of the standards and the uncertainty of the nominal value of the standard material. For transformation of nuclide ratios into specific activities in disintegration per minute (dpm) per kg, Al and Ca concentrations of Table S2 (1.13% Al; 1.08% Ca) have been used. For comparison of these specific activities measured by IAMS with Monte Carlo calculation based radius- and depth-dependent production rates (Leya & Masarik, 2009), additional values of Table S2 with data from Alexander (2019) and Lodders and Fegley (1998) have been used as input parameters.

### *Considerations Concerning Cosmogenic Nuclides*

Helium is purely cosmogenic (cos) except for additional radiogenic (rad)  $^4\text{He}$ . The former correlates with the lack of evidence for a Ne-trapped (tr) component. Thus, we can exclude the presence of a solar wind component. The  $^{36}\text{Ar}/^{38}\text{Ar}$  values for both samples ( $3.498 \pm 0.022$  for Elmsborn 1 and  $3.458 \pm 0.017$  for Elmsborn 2) do not match pure cosmogenic compositions

(0.63–0.67; Wieler, 2002); this implies mixing between trapped and cosmogenic Ar, which were separated with a two-component deconvolution between  $(^{36}\text{Ar}/^{38}\text{Ar})_{\text{cos}}$  and  $(^{36}\text{Ar}/^{38}\text{Ar})_{\text{tr}}$ . In the absence of solar wind He and Ne, the trapped component used in the deconvolution was constrained between the values for Q and air (5.32–5.34; Busemann et al., 2000; Nier, 1950).

### *Production Rates and Cosmic Ray Exposure Ages*

In order to calculate the cosmic ray exposure (CRE) age, the production rates of cosmogenic  $^3\text{He}$ ,  $^{21}\text{Ne}$ , and  $^{38}\text{Ar}$  must first be determined. This was done by using the model for OCs from Leya and Masarik (2009). This model takes into account the preatmospheric size of the meteoroid, the depth of the sample within the meteoroid, and the bulk chemical composition of the sample (see next). Both meteoroid size and sample depth are constrained using the measured purely cosmogenic  $^{22}\text{Ne}/^{21}\text{Ne}$  ratios as a shielding factor. A single production rate was defined from the two aliquots because their  $^{22}\text{Ne}/^{21}\text{Ne}$  ratios overlap within error (see next; Noble Gas Composition Section). The error-weighted mean of the two  $^{22}\text{Ne}/^{21}\text{Ne}$  ratios from Elmsborn 1 and 2 ( $1.1112 \pm 0.0038$ ) yielded several matches with the model predictions, ranging from radii of 25–500 cm. While the matches were mostly contained within depths of 6–10 cm for the lower radii, they shifted toward the center of the meteoroid at a radius of 120 cm. These deeper positions are statistically highly unlikely to host the sample (Mertens et al., 2021). Given the amount of material found, we also estimate that it would be unrealistic for the meteoroid to have exceeded a radius of 50 cm. For example, given a density of  $3.448 \text{ g cm}^{-3}$  for fragment E03 (see next; Density Measurements Section) and if only 1% (in this case, the totally found mass of 4277 g) of the preatmospheric material had survived atmospheric entry, the radius of the meteoroid would have been  $\sim 30$  cm. We consider this 99% ablation thought experiment to be an uncommon case, knowing that the average ablation for OCs with a radius  $\leq 60$  cm is of 91.5% of the preatmospheric material (Alexeev, 2003). The hypothesis of a relatively small preatmospheric radius along with our derived depths of samples match well with the values measured for  $^{26}\text{Al}$  and  $^{60}\text{Co}$  (see below in Further Short- and Long-Lived Radionuclides by Gamma Spectrometry Section; Alexeev et al., 2001; Kohout et al., 2017), which allows us to set an upper value for the radius at 50 cm. The derived meteoroid size, depth of samples, and production rates are given in Cosmic Ray Exposure Ages Section.

### *U/Th-He and K-Ar Gas Retention Ages*

The gas retention ages for Elmsborn 1 and 2 were calculated with both U/Th-He and K-Ar chronometers, with the U, Th, and K values measured on the



ICP-SFMS (see [Bulk Chemical Characteristics](#) Section). The  ${}^4\text{He}_{\text{rad}}$  values used in the U/Th-He chronometer were calculated with the safe assumption that the measured  ${}^3\text{He}$  concentrations were purely cosmogenic and applying a  $({}^4\text{He}/{}^3\text{He})_{\text{cos}}$  ratio between 5.2 and 6.1 (Wieler, 2002). The resulting  ${}^4\text{He}_{\text{cos}}$  concentration was then deducted from our measured  ${}^4\text{He}$  concentration (considering negligible  ${}^4\text{He}_{\text{tr}}$ ). The  ${}^{40}\text{Ar}_{\text{rad}}$  values used in the K-Ar chronometer were derived from the deconvoluted  ${}^{36}\text{Ar}_{\text{tr}}$  and a ratio  $({}^{40}\text{Ar}/{}^{36}\text{Ar})_{\text{tr}}$  between 0 and 295.5 (covering both Q and air composition; Busemann et al., 2000; Steiger & Jäger, 1977).

### *Radionuclides by Gamma Spectrometry*

Cosmogenic as well as primordial radionuclide concentrations were analyzed on the complete pieces of E01 (3731 g) and E02 (233.5 g) by nondestructive gamma spectrometry in the underground laboratory Felsenkeller (Niese et al., 1998) of the VKTA Rossendorf (Dresden).

The laboratory is situated under a rock overburden of 140 m w.e. (water equivalent), resulting in a suppression of the total muon intensity by a factor of 30–40 (Ludwig et al., 2019). Gamma spectrometry systems dedicated to the analysis of low- and very low-activity levels were utilized. Sample E01 was measured on a high-purity germanium (HPGe) detector of 31% relative efficiency. A shielding consisting of 8.5 cm electrolytic copper plus 3.0 cm low-activity and 12.0 cm standard lead was used for the measurements. The spectrometer applied for E02 is based on a coaxial p-type detector of 95% relative efficiency with enhanced front-side sensitivity for low-energy gamma rays. All construction elements were selected for low radioactivity. The passive shielding is graded and consists of 10 cm of electrolytic copper, 10 cm of low-activity lead ( $2\text{ Bq kg}^{-1} {}^{210}\text{Pb}$ ), and an outer layer of 10 cm lead with  $6\text{ Bq kg}^{-1} {}^{210}\text{Pb}$ . Up to 2011, the gamma spectrometry system was operated in the UDO laboratory in the Asse salt mine near Braunschweig; it was moved to Dresden in 2014. Detailed information about the gamma spectrometry system can be found in Neumaier et al. (2009). Both gamma spectrometry systems are flushed with vaporized nitrogen to suppress the influence of radon daughter nuclides from the laboratory air.

The nondestructive gamma spectrometric measurement of the E01 mass was carried out in the period August 16 and September 25, 2023 over a total time of 37 days. E02 fragment started on May 4, 2023 (10 days after the bolide event), and continued until June 4, 2023, resulting in a total measurement time of 27 days. Several minor breaks due to device maintenance lasted not longer than 1 day in total. To allow for a more precise radionuclide determination, the energy-dependent detection efficiency of the detector was determined in both cases with the measurement of a meteorite dummy made

of material with known naturally occurring radionuclide contents.

Gamma lines were detected from members of the natural decay series of the primordial nuclides  ${}^{238}\text{U}$  and  ${}^{232}\text{Th}$ , as well as  ${}^{40}\text{K}$  and short-lived cosmogenic nuclides. All given specific activities in units of disintegration per minute (dpm) per kg were corrected to April 25, 2023, 14:14, including decay correction during each measuring period itself.

### *Magnetic Properties*

The magnetic properties of the rock were studied in Aix-en-Provence and in Nördlingen. In Nördlingen, the MS of all available fragments was measured with the handheld device SM-30 from ZH Instruments ([www.zhinstruments.cz](http://www.zhinstruments.cz)).

In addition, magnetic measurements on three subsamples from two different specimens (E03 and E07; Table S1) were performed at CEREGE (Aix-en-Provence, France). Hysteresis measurements were performed with a Lake Shore 8604 vibrating sample magnetometer (VSM) with a sensitivity of  $\sim 5 \times 10^{-9}\text{ Am}^2$ . The analysis of hysteresis loops provided the ratio of saturation remanent magnetization ( $M_{\text{RS}}$ ) to saturation magnetization ( $M_{\text{S}}$ ) and the coercive force ( $B_{\text{C}}$ ). The errors concerning the obtained data on Elmshorn fragments are negligible. High-field susceptibility ( $\chi_{\text{HF}}$ ) was determined by a linear fit for applied fields between 1.2 and 1.5 T of the hysteresis loops. Remanent coercive force ( $B_{\text{CR}}$ ) was determined by back field experiments performed with the VSM. The low-field-specific susceptibility ( $\chi$  in  $\text{m}^3\text{ kg}^{-1}$ ) was measured using an Agico MFK1 apparatus with sensitivity of  $5 \times 10^{-13}\text{ m}^3$ , operating at  $200\text{ A m}^{-1}$ , and a frequency of 976 Hz. It was measured along three orthogonal axes to take the magnetic anisotropy into account. The coercivity spectrum was estimated up to 1.6 T through stepwise acquisition and measurement of isothermal remanent magnetization (IRM) using the VSM. We determined the  $S_{-300}$  ratio, defined as the ratio of the IRM obtained after applying a 3 T field and then a back field of 0.3 T, normalized to the IRM acquired in 3 T.

### *Micro-Fourier Transform Infrared Spectroscopy*

We used a Bruker Hyperion 3000 attached to a Bruker Vertex 80v located at the IR/IS facility at the Institut für Planetologie (University of Münster) to perform spectral measurements in specular reflectance mode on a thin section of the Elmshorn meteorite with a liquid nitrogen-cooled mercury–cadmium–tellurium detector and a 15× Cassegrain objective. An aperture of  $100 \times 100\ \mu\text{m}^2$  was set for each bulk measurement spot on areas of interests across the macroscopically distinct

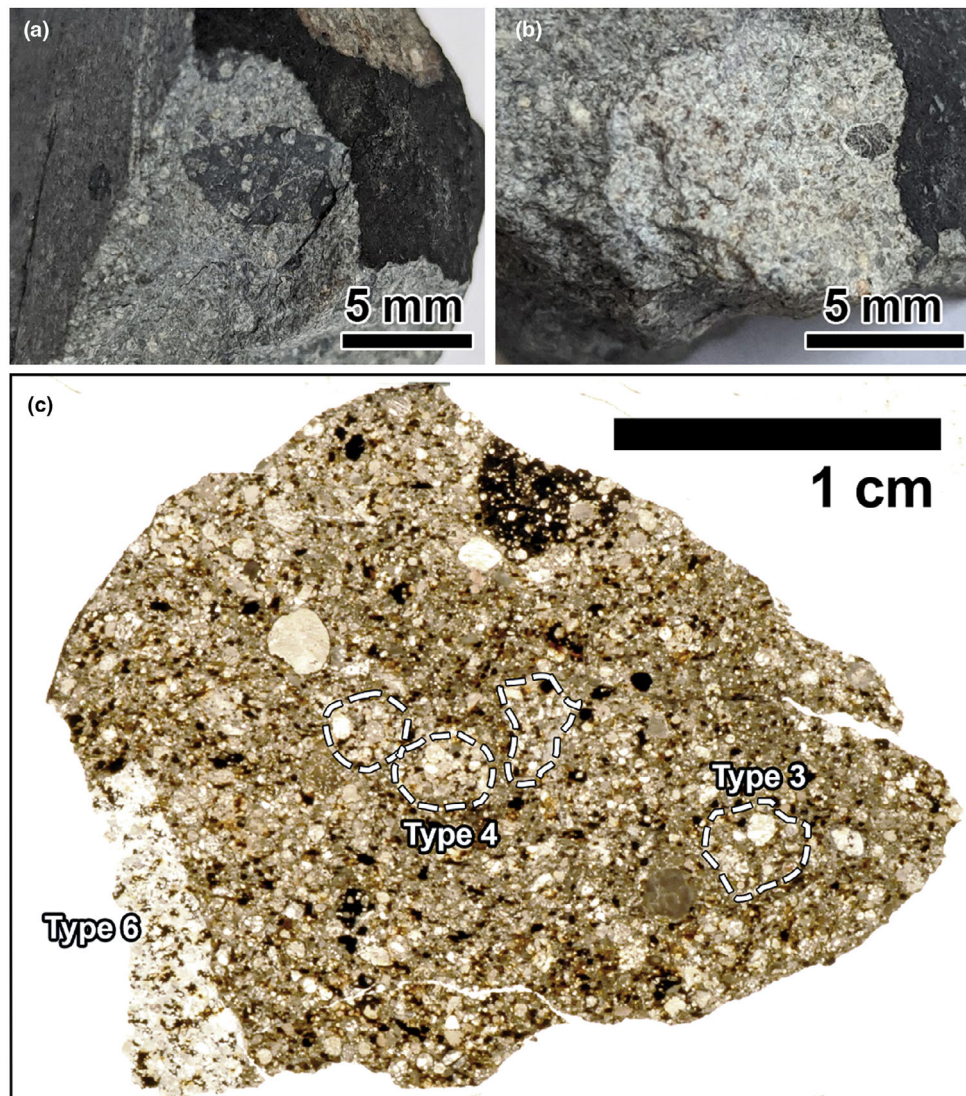


FIGURE 4. Inspection of the broken surfaces revealed the brecciated texture of the Elms horn fragment (E03) with (a) large light- and (b) dark-colored fragments embedded in a grayish clastic matrix. (c) A thin section shows various types of fragments in the clastic and dominating (medium light) groundmass, including parts of the dark (upper right) and light (type 6) fragments shown in (a) and (b), respectively. Some other small clasts are highlighted by white dashed lines.

lithologies of Elms horn fragment E07 (namely, the dark clast; Figure 4b,c, the coarse-grained light clast; Figure 4a,c, and the dominating clastic groundmass; Figure 4c) to obtain a specular reflectance signal. For each lithology, a minimum of  $2 \times 2$  measurement spots was applied in order to map a minimum sample area of  $400 \times 400 \mu\text{m}^2$ . All spectral information was acquired in the energetic range between  $2.5 \mu\text{m}$  ( $4000 \text{ cm}^{-1}$ ) and  $16.7 \mu\text{m}$  ( $600 \text{ cm}^{-1}$ ) and was averaged, resulting in one spectrum for each lithology. Spectral information obtained from the dark lithology of the meteorite was displayed as a single spot measurement, which was compared—based on the dark optical appearance—to the dark lithology of the Chelyabinsk meteorite. The

microscope was purged with dry air during measurements, as was the sample compartment, in order to avoid additional atmospheric interferences. All measurements were integrated over 512 scans to improve the signal-to-noise ratio, and the bulk measurements were smoothed with a Savitzky–Golay filter (10 pt). A suitable (i.e., a comparably flat) gold standard was used for calibration, and the spectral resolution was set to  $2 \text{ cm}^{-1}$ . All spectral data from the Elms horn samples will be available with the sample ID 609 Elms horn PL23029 in the Infrared and Raman for Interplanetary Spectroscopy (IRIS) database for space science missions (Weber et al., 2018). Spectral data that were used for comparison, for example, albite and Chelyabinsk dark

chip, ID 126 and ID 96, respectively, are already implemented and available in the IRIS database. The spectral data are available on the IRIS database at <http://bc-mertis-pi.uni-muenster.de/> and searchable either by ID number or name.

### Density

The density of the Elmshorn meteorite was measured by two different methods: In one approach, the bulk density of the rough piece (E02) of  $233.5 \pm 0.1$  g was determined in Augsburg with the method described by Consolmagno et al. (2008) using 40  $\mu\text{m}$  diameter glass beads. In another approach, the volumes of the same piece and of a different fragment (51.62 g from E03) were derived from X-ray computed tomography (CT) 3-D images and used for density calculations. Consistent results were obtained for the 233.5 g piece by both methods. For the largest fragment of Elmshorn (E01), the volume was obtained by digital optical techniques at the Digimold Reverse Engineering Company in Sonneberg (Germany).

### CT and Scanning

CT was performed three times: At the Helmholtz Institute Freiberg for Resource Technology, at the RIF e.V. (Dortmund), and at the private company 3D-MT in Augsburg (all in Germany).

In Freiberg, the Elmshorn meteorite sample (E02) of 233.5 g was scanned in a CoreTom CT scanner from Tescan. Two scans were performed, namely high-resolution region of interest (used in image S1) and low resolution (used to calculate the sample volume). The high-resolution image with a 20- $\mu\text{m}$  voxel size was obtained using an X-ray energy of 180 keV with a power of 20 W and one 0.5-mm thick copper filter mounted at the source. The low-resolution image with a 56- $\mu\text{m}$  voxel size was obtained using an X-ray energy of 180 keV with a power of 56 W and one 2-mm thick steel filter mounted at the source. The current used was optimized so that the resolution was limited by geometrical factors and not by the spot size of the beam. Reconstruction was done using the XRE recon v1.0.0.111. A beam-hardening correction of 0.12 was used to homogenize the gray scale throughout the samples. Image processing and visualization were done in Avizo 9.3.0. A 3-D nonlocal-means filter (window = 10, neighbor = 3, similarity = 0.7) was used in Figure S1 to remove noise with minimum impact on object boundaries.

In Dortmund, the interior of a piece of the 51.62 g Elmshorn fragment E03 was examined using a CT system manufactured by GE Sensing & Inspection (phoenix|x-ray vltomelx l 240D). The X-ray energy was 120 keV with a power of 12 W. Subsequent reconstruction was performed with filters to suppress artifacts and beam hardening using DATOS X-Reconstruction software (GE Sensing &

Inspection). The voxel size was  $\sim 25.6 \mu\text{m}$ , and subsequent visualization and analysis were performed using Dragonfly software from Comet Technologies Canada, Inc.

At 3D-MT in Augsburg (Germany), the smallest of the 21 recovered samples (E21), at 1.09 g, was scanned using a GE phoenix vltomelx m CT scanner with excellent resolution (voxel size 6.9165  $\mu\text{m}$ ).

### Find Locations

The stony meteorites were found at 21 different locations in the northern part of the city of Elmshorn (Figure 2). The three largest samples were found by the owners of their houses, while most of the smaller samples were found in inhabited terrain after an intensive effort by private searches. Two railway tracks intersect the strewn field; most of the small pieces were found northeast of the tracks. The typical landscape north of the tracks and within the inhabited terrain are shown in Figure 3.

## RESULTS

### Hand Specimen Characteristics

Currently, 21 pieces have been recovered in a strewn field of about  $2.5 \times 1.5 \text{ km}^2$  within a few weeks, totaling a mass of 4.282 kg (Figure 2; Table S1). Depending on the impact location, some fragments were perfectly preserved with a complete fusion crust (Figure 1), whereas others were smashed into many pieces. Upon inspection of the broken surfaces, the brecciated texture of Elmshorn was found to be perfectly presented (Figure 4). Within a dominating grayish groundmass, large light- and dark-colored fragments are easily recognized (Figure 4a,b). Thus, obviously, Elmshorn is a breccia consisting of a mixture of different lithologies. This textural characteristic is also observable in polished thin sections (Figure 4c).

### CT Observations

Some typical images from the interiors of the Elmshorn samples E02, E03, and E21 are presented in Figures S1–S3. The brecciated texture of Elmshorn is also visible during CT studies (Figures S1d and S2d). The metals and sulfides in Elmshorn are also found to be heterogeneously distributed (e.g., Figure S1b). In all studied pieces, millimeter-sized, elongated metal grains can be found (Figures S1–S3), as can remarkable metal–silicate intergrowths, which are probably related to shock-darkened fragments (Figure S2d). In such a case, metals and sulfides fill the cleavage planes, fractures, boundaries, and voids of the main silicates (mainly olivine and low-Ca pyroxene; compare Morlok et al., 2017).

## Mineralogy

The thin sections prepared from the broken fragment (E03; Figure 4c) show that the rock is a complex breccia consisting of equilibrated and recrystallized lithologies (types 4–6) as well as unequilibrated type 3 lithologies (Table 1; Figure 4). The boundaries of several large fragments are well defined (Figure 4); however, those of smaller fragments in the groundmass are difficult to detect. Overall, different types of chondrules are well preserved (Figure 6). Barred olivine (BO), radial pyroxene, and cryptocrystalline (C) chondrules are easily recognized, whereas porphyritic chondrules are less easy to detect but are present in several types 3 and 4 lithic clasts. In clasts of higher petrologic grade (types 5 and 6), they easily merge with the matrix due to metamorphic recrystallization. Some Al-rich chondrules are present (e.g., Bischoff & Keil, 1983a, 1983b, 1984; Ebert & Bischoff, 2016a). The example shown in Figure 6c,d is rich in Na<sub>2</sub>O and K<sub>2</sub>O and mainly consists of a Na,K,Al-rich mesostasis embedding zoned olivine (Fa<sub><1–27</sub>) and skeletal Al-Ti diopside (fassaite; Figure 6c,d; Table 2). On average, the mesostasis contains about 10.5 wt% Na<sub>2</sub>O, 5 wt% K<sub>2</sub>O, and 23 wt% Al<sub>2</sub>O<sub>3</sub> (Table 2). Olivine is by far the most abundant phase and heterogeneous in composition throughout all polished sections. The mean composition of 103 randomly and automatically analyzed olivines (grid analysis) was found to be Fa<sub>19.6±1.5</sub> with a compositional range between 14 and 24 mole% Fa (Table 1). However, a detailed search of individual olivines revealed a range between Fa<sub><1</sub> and Fa<sub>32</sub>. The random analysis of olivine shows that most grains plot at Fa<sub>19–20</sub>, but a significant number of olivines have Fa contents above 20 mole% (Figure 8). The 78 randomly analyzed low-Ca pyroxenes have compositions of Fs<sub>16.1±2.4</sub>Wo<sub>1.6±1.4</sub> (Table 1) and the Fs contents vary between 9 and 24 mole%. Plagioclase analyses were mainly obtained from the large H6 fragment (compare Figure 4), revealing a mean composition of An<sub>11.3</sub>Ab<sub>86.6</sub>Or<sub>2.1</sub> (Table 1). Based on their size, chromites and phosphates were also easily found and analyzed in the metamorphosed clasts. The apatites were found to be rich in Cl (5.5–6.2 wt%) and similar in composition to those reported from Ward et al. (2017) for many other OCs. However, they are different from apatites found in the recently analyzed Renchen L OC breccia, which have 3.4 wt% F (Bischoff, Barrat, et al., 2019). The merrillites have, on average, 2.9 wt% Na<sub>2</sub>O and 3.6 wt% MgO (Table 2). Chromites are relatively homogeneous in composition, with 57.1 ± 0.40 wt% Cr<sub>2</sub>O<sub>3</sub> and 29.3 ± 0.47 wt% FeO (Table 2). Metals and sulfides are abundant throughout all the thin sections, and their mean compositions are given in Table 3. Kamacite is certainly more abundant than taenite. The Ni and Co concentrations of kamacite vary (2.0–8.0 wt% and 0.64–

0.80 wt%, respectively). Frequently, kamacites were found to have relatively low Ni concentrations of about 2–4 wt%. The taenite composition was found to vary, with Ni content varying between 17 and 39 wt% (mean: 29.2 wt%) and Co concentrations between 0.13 and 0.67 wt% (mean: 0.35 wt%); however, we cannot rule out that this observation reflects the analyses of fine-grained intergrowths of taenite and kamacite. Some grains of tetraenaite (~Fe<sub>50</sub>Ni<sub>50</sub>) were also detected. The sulfide is pure troilite with 35.9 wt% S and 61.7 wt% Fe (Table 3).

For comparison, olivine and low-Ca pyroxene within a second sample (E07) of the strewn field were analyzed (grid analysis). Within this sample, the mean composition of 106 randomly analyzed olivines was found to be Fa<sub>20.7±2.3</sub> with a compositional range between 10 and 32 mole% Fa (Table 1; Figure 8). The coexisting low-Ca pyroxene was found to have a mean composition of Fs<sub>16.2±2.8</sub>En<sub>83.0±3.0</sub>Wo<sub>0.8±0.6</sub> (*n* = 79) with a range between 5 and 24 mole% Fs.

When viewed in detail, the mineralogy of Elmshorn is more complex than indicated by the randomly obtained data on the mineral chemistry. Within the studied thin sections, most obvious lithologies are a light, strongly recrystallized (type 6) fragment (Figure 4) and a fine-grained dark clast (Figures 4 and 7). Olivine (Fa<sub>19.6±0.32</sub>; *n* = 18) and low-Ca pyroxene compositions (Fs<sub>15.5±0.5</sub>Wo<sub>1.4±0.2</sub>) of the light clast clearly plot into the field for H chondrites (Figure 8). Plagioclase grains in the clast reach sizes of up to about 100 μm. Some large chromites, apatites, and troilites also occur (Tables 1–3). The kamacite grains contain 5.8 wt% Ni and 0.71 wt% Co, on average (Table 3). The Co concentrations are somewhat higher than those given by Rubin (1990; ~0.5 wt%).

The dark clast has abundant fine-grained material embedding a low abundance of chondrules and chondrule fragments. The textural characteristics (Figure 7b) resemble those of impact melts, but distinct differences exist. The most significant difference is the skeletal shape of the metals (Figure 7b), which are spherulitic in typical impact melt rocks. Within the dark clast, the small metal grains in the fine-grained groundmass are homogeneously distributed and skeletal in shape. Their occurrence is probably responsible for the dark appearance of the clast in transmitted light (Figures 4 and 7). The compositions of olivine (Fa<sub>20.2±0.4</sub>; *n* = 18; Table 1; Figure 8) are rather constant and the low-Ca pyroxenes (Fs<sub>15.9±1.8</sub>Wo<sub>0.8±0.3</sub>) vary moderately, as is often observed in H4 chondrites since the equilibration of olivine is faster than that of low-Ca pyroxene. The composition of the matrix olivine is ~Fa<sub>20.5</sub>.

A 2-mm-sized, large clast of an unusual melt is an eye-catching component in one of the thin sections (Figure 5f). The silicate-rich object contains skeletal

TABLE 1. Mean chemical composition of the main silicates in the Elmshorn bulk rock E03 (bulk-1) and of olivine from some of its fragments (exception: olivine-bulk-2 is from fragment E07).

	Olivine (bulk-1) ( <i>n</i> = 103)	Low-Ca Px (bulk-1) ( <i>n</i> = 78)	Plagioclase <sup>a</sup> (bulk-1) ( <i>n</i> = 16)	Olivine (bulk-2) ( <i>n</i> = 106)	H6 clast olivine ( <i>n</i> = 18)	Dark clast (H) olivine ( <i>n</i> = 18)	H/L3.9 clast Frag H ( <i>n</i> = 16)	H/L4 clast Frag G ( <i>n</i> = 15)	H/L3.9 clast Frag A ( <i>n</i> = 17)	H/L3.9 clast Frag B ( <i>n</i> = 19)	H/L4 clast Frag F ( <i>n</i> = 17)
SiO <sub>2</sub>	39.0 ± 0.6	56.1 ± 1.0	65.5 ± 0.8	39.0 ± 0.7	38.8 ± 0.2	38.7 ± 0.4	38.8 ± 0.2	38.3 ± 0.4	38.5 ± 0.3	38.5 ± 0.3	38.5 ± 0.2
Al <sub>2</sub> O <sub>3</sub>	<0.02	0.43	20.3 ± 0.5	<0.02	<0.01	<0.01	n.d.	<0.02	<0.02	<0.01	<0.01
Cr <sub>2</sub> O <sub>3</sub>	0.05	0.29	<0.03	0.04	0.03	0.04	<0.04	<0.03	<0.03	<0.02	0.05
FeO	18.2 ± 1.3	10.7 ± 1.5	0.53 ± 0.2	19.4 ± 2.0	18.4 ± 0.3	18.9 ± 0.4	19.5 ± 1.0	19.9 ± 1.0	20.4 ± 1.1	19.9 ± 1.2	19.4 ± 0.6
MnO	0.44 ± 0.05	0.47 ± 0.11	<0.01	0.47 ± 0.05	0.46 ± 0.04	0.46 ± 0.3	0.39 ± 0.07	0.45 ± 0.05	0.44 ± 0.04	0.48 ± 0.04	0.45 ± 0.04
MgO	41.6 ± 1.2	30.7 ± 1.7	0.19	41.5 ± 1.8	42.1 ± 0.5	41.7 ± 0.4	41.0 ± 0.9	40.5 ± 0.9	40.1 ± 0.9	40.6 ± 1.0	40.9 ± 0.5
CaO	0.03	0.80 ± 0.70	2.41 ± 0.4	0.03	<0.02	<0.02	<0.02	<0.02	<0.03	<0.01	<0.02
Na <sub>2</sub> O	<0.01	0.08	10.2 ± 0.4	<0.01	<0.01	<0.01	<0.02	<0.02	<0.01	<0.01	<0.01
K <sub>2</sub> O	<0.01	<0.01	0.37 ± 0.2	<0.01	<0.01	<0.02	<0.02	<0.01	<0.01	<0.01	<0.01
P <sub>2</sub> O <sub>5</sub>	<0.03	<0.01	<0.02	<0.02	<0.02	<0.02	<0.04	0.05	n.a.	n.a.	n.a.
Total	99.39	99.59	99.56	100.50	99.86	99.88	99.83	99.30	99.54	99.54	99.35
Fa	19.6 ± 1.5			20.7 ± 2.3	19.6 ± 0.3	20.2 ± 0.4	21.0 ± 1.2	21.5 ± 1.0	22.0 ± 1.3	21.5 ± 1.4	20.9 ± 0.7
Te	0.49 ± 0.06			0.52 ± 0.05	0.50 ± 0.04	0.50 ± 0.03	0.43 ± 0.07	0.50 ± 0.05	0.49 ± 0.04	0.52 ± 0.04	0.49 ± 0.04
Fs		16.1 ± 2.4									
Wo		1.6 ± 1.4									
An			11.3 ± 2.2								
Or			2.1 ± 0.8								

Note: All data in wt%.

Abbreviations: *n*, number of analyses; n.a., not analyzed; n.d., not detected; Plag, plagioclase; Px, pyroxene; Te, tephroite (Mn) component in olivine.

<sup>a</sup>Mostly plagioclase from the H6 clast.

TABLE 2. Chemical composition of minor phases in the Elmshorn breccia E03 as well as the bulk composition and (contaminated) phases of the melt fragment M from E03 (Figure 5f and Figure S1). Mesostasis and fassaite from the Na,Al-rich chondrule shown in Figure 6c,d.

						Melt fragment M			
	Mesostasis (bulk) ( <i>n</i> = 5)	Fassaite (mean) ( <i>n</i> = 2)	Apatite ( <i>n</i> = 5) <sup>a</sup>	Merrillite ( <i>n</i> = 6)	Chromite ( <i>n</i> = 8)	Bulk chem ( <i>n</i> = 397)	Olivine ( <i>n</i> = 20)	Low-Ca pyroxene ( <i>n</i> = 16)	Ca pyroxene ( <i>n</i> = 6)
SiO <sub>2</sub>	57.5 ± 2.8	52.7	0.14	0.09	0.23 ± 0.15	45.0	39.0 ± 0.4	54.1 ± 0.9	49.3 ± 0.7
TiO <sub>2</sub>	0.90 ± 0.08	0.93	<0.03	<0.01	2.33 ± 0.27	0.27	0.12	0.38	0.72
Al <sub>2</sub> O <sub>3</sub>	23.0 ± 1.4	21.9	<0.04	<0.01	6.1 ± 0.64	6.4	1.03 ± 0.34	12.0 ± 0.6	6.2 ± 0.9
Cr <sub>2</sub> O <sub>3</sub>	0.27 ± 0.14	0.55	0.18	0.07	57.1 ± 0.40	0.47	0.32	0.52	1.06
FeO	1.56 ± 0.57	2.21	0.60	0.66	29.3 ± 0.47	16.1	23.0 ± 1.3	9.3 ± 1.1	8.8 ± 0.8
MnO	n.d.	<0.02	n.d.	n.d.	0.96 ± 0.15	0.35	0.51	0.21	0.37
MgO	0.30 ± 0.46	5.8	0.05	3.6	3.1 ± 0.34	23.7	36.4 ± 1.4	15.1 ± 0.9	15.5 ± 0.8
CaO	0.51 ± 0.58	15.9	51.2	45.6	0.11	3.4	0.19	2.7 ± 0.4	17.2 ± 1.3
Na <sub>2</sub> O	10.5 ± 2.7	n.d.	0.41	2.88	0.22	2.49	0.44	5.3 ± 0.5	0.44
K <sub>2</sub> O	5.0 ± 2.7	n.d.	0.06	n.d.	<0.02	0.12	<0.01	0.25	n.d.
P <sub>2</sub> O <sub>5</sub>	0.16 ± 0.07	n.d.	41.4	47.3	<0.03	Ni: 0.09	n.a.	n.a.	n.a.
Total	99.43	100.01	99.91 <sup>a</sup>	100.22	99.50 <sup>b</sup>	98.39	101.02	99.86	99.59
							Fa: 26.0		

Note: Most chromites from the H6 fragment. All data in wt%.

Bold indicates the results of this study and italics indicates the mean of many literature data.

Abbreviations: *n*, number of analyses; n.a., not analyzed; n.d., not detected; Plag, plagioclase.; Px, pyroxene.

<sup>a</sup>Contains 5.8 wt% Cl.

<sup>b</sup>Not analyzed for Zn, V, etc., and not checked for Fe<sup>3+</sup>.

TABLE 3. Mean chemical composition of metals and sulfide (troilite) from Elmshorn fragment E03.

	Elmshorn (bulk sample)				Elmshorn (H6 fragment)	
	Kamacite ( <i>n</i> = 26)	Taenite ( <i>n</i> = 5)	Troilite ( <i>n</i> = 12)	Tetrataenite ( <i>n</i> = 1)	Kamacite ( <i>n</i> = 5)	Troilite ( <i>n</i> = 3)
Fe	93.3 ± 0.96	70.1 ± 10.2	61.7 ± 0.55	48.5	93.0 ± 1.3	62.6 ± 0.1
Co	0.69 ± 0.06	0.35 ± 0.23	0.10 ± 0.03	0.12	0.71 ± 0.05	0.08 ± 0.03
Ni	5.4 ± 1.33	29.2 ± 10.2	0.03 ± 0.03	49.2	5.8 ± 1.3	<0.03
S	n.d.	n.d.	35.9 ± 0.28	n.d.	n.d.	36.0 ± 0.3
Total	99.39	99.65	97.73	97.82	99.51	98.71

Note: All data in wt%.

Abbreviation: n.d., not detected.

crystals (olivine, pyroxenes) embedded in a fine-grained groundmass. The bulk composition of the so-called melt clast is given in Table 2. The almost equilibrated olivines (Fa<sub>26</sub>; Table 2) contain considerable concentrations of Al<sub>2</sub>O<sub>3</sub> (1.03 wt%) and Na<sub>2</sub>O (0.44 wt%). Also, the coexisting pyroxenes have unusual compositions with remarkably high concentrations of Al<sub>2</sub>O<sub>3</sub> and Na<sub>2</sub>O (Table 2), which may be the result of contamination due to the fine-grained intergrowths of different phases (Figure S4).

As stated earlier during randomly selected mineral analysis, olivines with Fa contents above 20 (up to 24) mol % were frequently encountered, and a detailed search revealed olivine compositions ranging from Fa<sub><1</sub> to Fa<sub>32</sub>. The olivines with highly variable Fa contents can be assigned to type 3 fragments, in which chondrules have glassy mesostasis (Figures 5 and 6) and strongly zoned

olivine and low-Ca pyroxene crystals (Figure 6d). In BSE images from the Elmshorn main portion, areas were detected that show up as slightly lighter gray than others (Figure S5). Detailed studies revealed that they represent distinct clasts with almost equilibrated olivine compositions (often type 3.8–4). The mean Fa contents are well above 20 mole%, indicating an H/L or L chondrite origin (Figure 8). Some fragments were identified and analyzed with almost equilibrated olivines having (mean) Fa<sub>21.0±1.2</sub>, Fa<sub>21.5±1.0</sub>, Fa<sub>22.0±1.3</sub>, Fa<sub>21.5±1.4</sub>, and Fa<sub>20.9±0.7</sub> (Figure 8). These fragments must be of an intermediate H/L chondrite heritage.

As mentioned earlier, the studied section of the second analyzed stone (E07) has lithic clasts with abundant olivine of Fa<sub>21–23</sub> (Figure 8b). These olivines are significantly FeO richer than those in the E03 piece. Thus, the typical H chondrite lithologies (with Fa<sub>18–20</sub>) are less

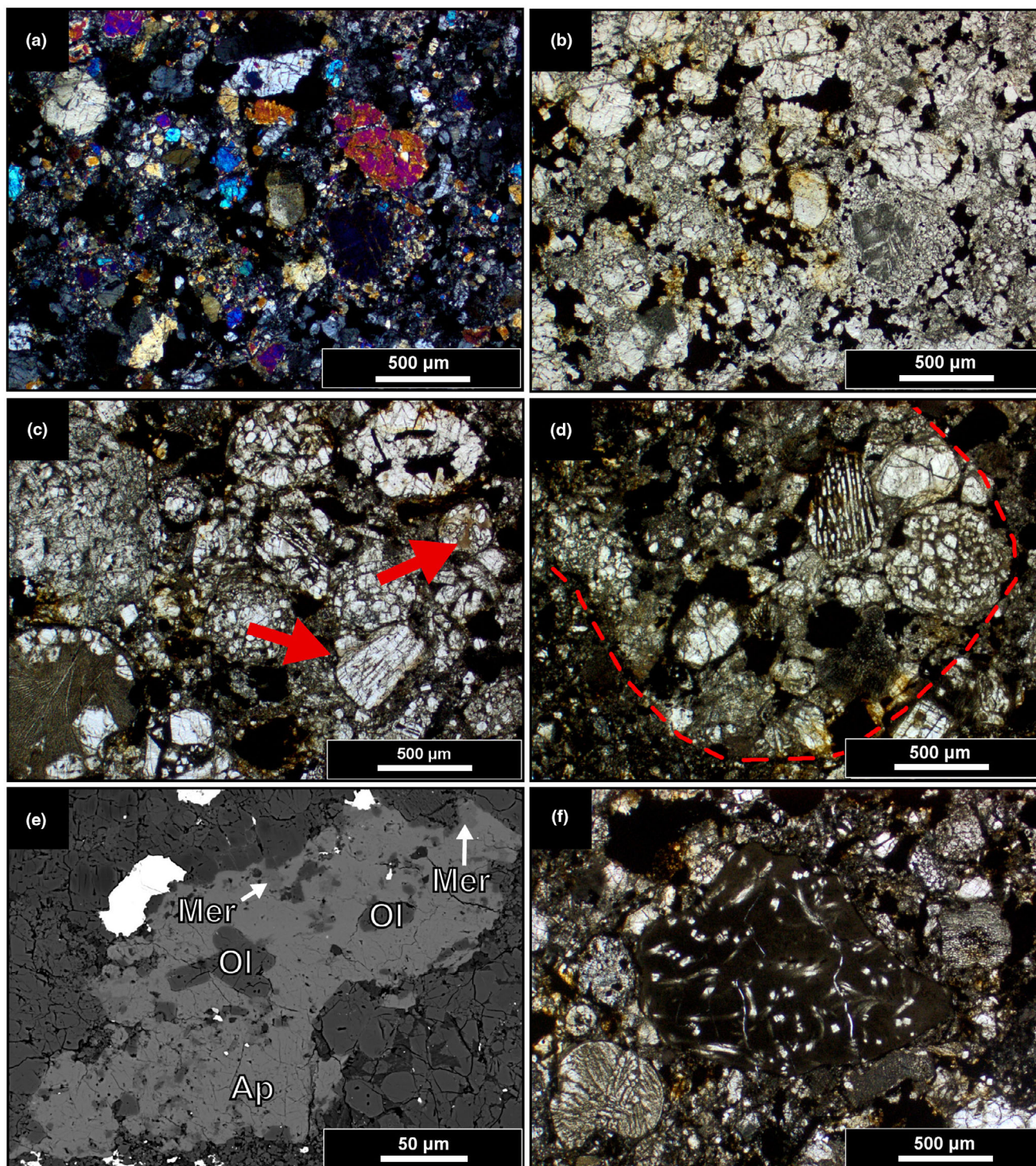


FIGURE 5. Lithologies from E03: (a) type 6 clast in transmitted polarized light (crossed nicols); (b) same clast as in (a) in-plane polarized light; (c) type 3 fragment with chondrules containing brownish mesostasis glass (arrows; plane polarized light); (d) type 4 fragment enclosed in the fine-grained, clastic matrix; the dashed line indicates the boundary of the clast (plane polarized light); (e) large association with apatite (Ap), olivine (Ol;  $\sim\text{Fa}_{17.5}$ ), and merrillite (Mer) in the matrix of Elmshorn (BSE image); (f) large clast (fragment M) of an unusual melt with skeletal crystals (partly olivine  $[\text{Fa}_{26}]$ ) embedded in a fine-grained groundmass (plane polarized light).

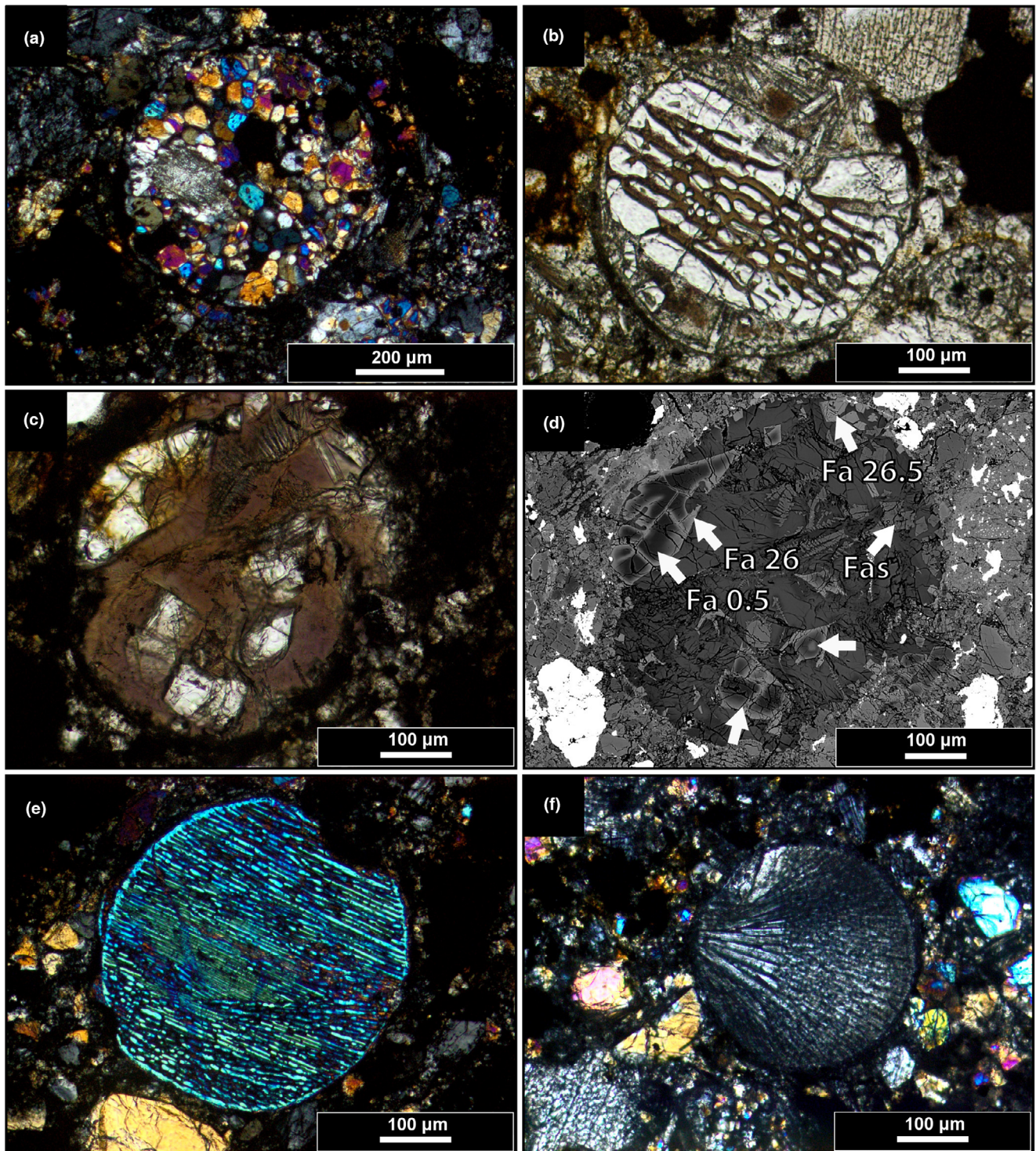


FIGURE 6. Chondrules from E03: (a) olivine- and pyroxene-rich (POP) chondrule; (b) barred olivine (BO) chondrule with interstitial mesostasis glass (brownish); (c) Na,Al-rich chondrule with olivine and pyroxenes enclosed in Al-rich brownish mesostasis; (d) same chondrule as in (c), arrows indicate the strong zoning of olivine ( $Fa_{<1-27}$ ) as well as the occurrence of Ca pyroxene (fassaite [Fas]); (e) BO chondrule; (f) radial pyroxene (RP) chondrule. Figures in transmitted light except for the BSE image in (d).



TABLE 4. Oxygen isotope composition of eight aliquots from the Elmshorn chondrite breccia. Four samples of the shattered rock E03 were analyzed as well as four aliquots of E07 found to the northeast of E03.

Meteorite	Sample	Mass (mg)	$\delta^{17}\text{O}$	$\delta^{18}\text{O}$	$\Delta^{17}\text{O}$
Elmshorn	E03: sample-1	2.251	2.614	3.831	0.592
Elmshorn	E03: sample-2	2.062	2.937	4.051	0.799
Elmshorn	E03: sample-3	2.144	2.667	4.018	0.546
Elmshorn	E03: sample-4	2.037	3.079	4.511	0.698
	<i>Mean</i>		2.824	4.103	0.659
Elmshorn	E07: sample-1	2.090	2.788	3.735	0.815
Elmshorn	E07: sample-2	2.246	2.839	4.097	0.676
Elmshorn	E07: sample-3	2.153	2.845	4.187	0.635
Elmshorn	E07: sample-4	2.030	2.754	4.018	0.634
	<i>Mean</i>		2.807	4.009	0.690

abundant in sample E07 than in sample E03. Some typical images from sample E07 are given in Figure S6.

### Shock Metamorphism of Elmshorn

The studied thin sections of the Elmshorn OC clearly show that the rock is a complex breccia. In order to determine the shock degree of a bulk rock breccia, the fragment with the lowest degree of shock has to be considered. Thus, Elmshorn has a shock degree of S2 (C-S2) considering the undulatory extinction of olivines in many lithic clasts (Bischoff, Schleiting, et al., 2019; Bischoff & Stöffler, 1992; Stöffler et al., 1991, 2018). Since the brecciated character of Elmshorn is easily detectable in the hand specimen and clearly visible in thin sections (Figure 4), individual clasts certainly exist that have a higher degree of shock metamorphism than S2. Fragments with olivines having planar fractures exist as well as fragments showing typical characteristics of shock darkening (Figure 9c) or clasts having internal shock veins. We also detected thin, but several millimeter-long metal-sulfide associations that may have been formed due to shock processes (Figure 9f, Figures S1 and S2) as well as porous vein-like areas with unusual metal and sulfide constituents (Figure 9e). Finally, clasts of impact melt veins or pools (Figure 9a) and the dark clasts with the internal, fine-grained distribution of metals and sulfides (Figure 9b) indicate a complex impact-related history.

### Oxygen Isotopes

The O isotope compositions of the eight analyzed chips from two different fragments are listed in Table 4. The sample E03 is dominated by H chondrite components, and sample E07 has physical properties (density, MS) consistent with L chondrites. However, all data for the two Elmshorn fragments plot within the field of H chondrites and are indistinguishable from each other (Figure 10).

### Bulk Chemical Characteristics

For most elements, the chemical compositions of Elmshorn (Table 5) are close to the compositions of the recently analyzed meteorites Ejby, Blaubeuren, Braunschweig, Antonin, L'Aigle, and Saint-Pierre-le-Viger and are also similar to the mean composition of L and H chondrites (Bartoschewitz et al., 2017; Bischoff, Barrat, et al., 2019; Bischoff, Patzek, et al., 2022a; Bischoff et al., 2023; Lodders & Fegley, 1998). The relatively high concentrations of Fe, Co, and Ni in the Elmshorn sample E03 are clearly more related to other H chondrites than to L chondrites.

### Titanium and Chromium Isotopes

The nucleosynthetic Ti isotope data of Elmshorn, BHVO-2, and Forest Vale are listed in Table 6. The Ti isotope composition of Elmshorn shows an isotopic deficit in  $\epsilon^{46}\text{Ti}$  and  $\epsilon^{50}\text{Ti}$  data relative to Earth ( $\epsilon^i = 0$ ), which agrees with the data of the Forest Vale OC (H4) and generally with those of OCs from the literature (Figures 11 and 12). The nucleosynthetic Cr isotope values for Elmshorn and DTS-2 are shown in Table 6. The Elmshorn Cr isotope data show an excess in  $\epsilon^{53}\text{Cr}$  and a deficit in  $\epsilon^{54}\text{Cr}$ , relative to the terrestrial composition, again in agreement with OC literature values (Figure 12). The Ti and Cr isotope data thus indicate that the Elmshorn meteorite originated in the NC (noncarbonaceous meteorite) reservoir in the inner solar system and that it belongs to the group of OCs.

### Noble Gas Composition

The presence of a solar wind component can be excluded for both aliquots because trapped components are not distinguishable for both He and Ne (Table 7a). Thus, Elmshorn is a fragmental breccia. As stated earlier, the Ar values are composed of a mixture between both cosmogenic and trapped Ar with the addition of  $^{40}\text{Ar}_{\text{rad}}$  (Table 7b). The trapped component cannot be further narrowed down since the Q and air  $^{36}\text{Ar}/^{38}\text{Ar}$  ratios are isotopically too close. The Kr and Xe isotopes show mainly trapped signatures (Table 7b,c). The Xe-trapped component for the two aliquots is dominated by Q, as shown in Figure 13, which suggests that both Ar and Kr are also from phase Q. The noticeable deviation from the Q composition of the  $^{124}\text{Xe}/^{132}\text{Xe}$  ratios for both samples implies a small cosmogenic influence. Both Elmshorn 1 and 2 (both subsamples from E03) show short-lived  $^{129}\text{I}$ -derived  $^{129}\text{Xe}$  excesses. This feature is usually seen in OCs of types 5 or 6 (e.g., Alaerts et al., 1979; Moniot, 1980).

TABLE 5. Major and trace element abundances of the anomalous (an) Elmshorn H3-6 chondrite breccia (sample E03). The mean of about 1600 randomly obtained microprobe analyses on two Elmshorn samples revealed Al and Si concentrations of 1.38 and 18.6 wt%, respectively.

Element	Ejby H5/6	Blaubeuren H5-6	Mean H	Elmshorn H3-6-an	Mean L	Braunschweig L6	Antonin L4-5
Al	1.10 <sup>a</sup>	1.05 <sup>a</sup>	<b>1.06<sup>a</sup></b>		<b>1.16<sup>a</sup></b>	1.159 <sup>a</sup>	1.01 <sup>a</sup>
Fe	28.7 <sup>a</sup>	24.5 <sup>a</sup>	<b>27.2<sup>a</sup></b>	<b>31.7<sup>a</sup></b>	<b>21.8<sup>a</sup></b>	21.6 <sup>a</sup>	22.0 <sup>a</sup>
Mg	14.99 <sup>a</sup>	13.28 <sup>a</sup>	<b>14.1<sup>a</sup></b>	<b>12.6<sup>a</sup></b>	<b>14.9<sup>a</sup></b>	15.0 <sup>a</sup>	14.4 <sup>a</sup>
Na	0.67 <sup>a</sup>	0.25 <sup>a</sup>	<b>0.61<sup>a</sup></b>	<b>0.60<sup>a</sup></b>	<b>0.69<sup>a</sup></b>	0.712 <sup>a</sup>	0.65 <sup>a</sup>
Ni	2.11 <sup>a</sup>	1.57 <sup>a</sup>	<b>1.71<sup>a</sup></b>	<b>2.05<sup>a</sup></b>	<b>1.24<sup>a</sup></b>	1.23 <sup>a</sup>	1.56 <sup>a</sup>
P	1309	812	<b>1200</b>	<b>1177</b>	<b>1030</b>	1310	905
K	950	421	<b>780</b>	<b>997</b>	<b>920</b>	1021	873
Ca	1.28 <sup>a</sup>	1.02 <sup>a</sup>	<b>1.22<sup>a</sup></b>	<b>1.08<sup>a</sup></b>	<b>1.33<sup>a</sup></b>	1.41 <sup>a</sup>	1.21 <sup>a</sup>
Sc	8.7	7.39	<b>7.8</b>	<b>4.4</b>	<b>8.1</b>	10.01	8.52
Ti	620	480	<b>630</b>	<b>581</b>	<b>670</b>	644	610
V	74	49.4	<b>73</b>	<b>73</b>	<b>75</b>	70.09	62.1
Cr	3118	3597	<b>3500</b>	<b>3573</b>	<b>3690</b>	3804	3048
Mn	2606	2036	<b>2340</b>	<b>2417</b>	<b>2590</b>	0.267 <sup>a</sup>	2478
Co	715	621	<b>830</b>	<b>1105</b>	<b>580</b>	601	582
Cu	73.1			<b>84</b>	<b>90</b>		84.6
Zn	43.5	25.6	<b>47</b>	<b>57</b>	<b>57</b>	43.96	42.4
Ga	5.06	4.46	<b>6.0</b>	<b>5.8</b>	<b>5.4</b>	5.05	4.81
Rb	2.88	1.17	<b>2.3</b>	<b>5.8</b>	<b>2.8</b>	3.06	2.59
Sr	10.9	5.58	<b>8.8</b>	<b>9.4</b>	<b>11</b>	11.34	10.5
Y	2.97	1.65	<b>2.0</b>	<b>2.1</b>	<b>1.8</b>	2.32	1.98
Zr	4.63	4.47	<b>7.3</b>	<b>4.8</b>	<b>6.4</b>	6.48	5.02
Nb	0.381	0.399	<b>0.4</b>	<b>0.59</b>	<b>0.4</b>	0.46	0.43
Cs	0.0178			<b>0.32</b>		0.048	0.030
Ba	3.49	2.06	<b>4.4</b>	<b>2.90</b>	<b>4.1</b>	3.78	3.53
La	0.344	0.226	<b>0.301</b>	<b>0.295</b>	<b>0.318</b>	0.328	0.277
Ce	0.885	0.599	<b>0.763</b>	<b>0.777</b>	<b>0.970</b>	0.873	0.711
Pr	0.132	0.089	<b>0.120</b>	<b>0.116</b>	<b>0.140</b>	0.128	0.107
Nd	0.658	0.450	<b>0.581</b>	<b>0.593</b>	<b>0.700</b>	0.649	0.538
Sm	0.211	0.147	<b>0.194</b>	<b>0.188</b>	<b>0.303</b>	0.218	0.176
Eu	0.072	0.064	<b>0.074</b>	<b>0.069</b>	<b>0.080</b>	0.0827	0.079
Gd	0.303	0.204	<b>0.275</b>	<b>0.266</b>	<b>0.317</b>	0.30	0.243
Tb	0.0548	0.0348	<b>0.049</b>	<b>0.048</b>	<b>0.059</b>	0.0549	0.045
Dy	0.369	0.262	<b>0.305</b>	<b>0.330</b>	<b>0.372</b>	0.378	0.306
Ho	0.0815	0.0586	<b>0.074</b>	<b>0.073</b>	<b>0.089</b>	0.0835	0.069
Er	0.239	0.174	<b>0.213</b>	<b>0.216</b>	<b>0.252</b>	0.250	0.302
Tm	0.0356	0.0270	<b>0.033</b>		<b>0.038</b>		0.031
Yb	0.228	0.178	<b>0.203</b>	<b>0.212</b>	<b>0.226</b>	0.256	0.206
Lu	0.0345	0.0274	<b>0.033</b>	<b>0.031</b>	<b>0.034</b>	0.0392	0.0313
Hf	0.135	0.135	<b>0.150</b>	<b>0.135</b>	<b>0.170</b>	0.197	0.152
Ta	0.0107	0.0163	<b>0.021</b>	<b>0.018</b>	<b>0.021</b>	0.0227	0.0216
Pb	0.057	0.0119	<b>0.240</b>	<b>0.67</b>	<b>0.040</b>	0.0336	0.0316
Th	0.0378	0.0308	<b>0.038</b>	<b>0.036</b>	<b>0.042</b>	0.0452	0.034
U	0.010	0.0080	<b>0.013</b>	<b>0.009</b>	<b>0.015</b>	0.0128	0.0102

Note: Data for two H chondrites (Ejby, Blaubeuren) and two L chondrites (Braunschweig, Antonin) for comparison. Literature data are from Haack et al. (2019), Bartoschewitz et al. (2017), Bischoff, Patzek, et al. (2022) and Bischoff, Storz, et al. (2022). The data for mean L and H chondrites are taken from Lodders and Fegley Jr. (1998).

<sup>a</sup>Data in wt%, other data in ppm.

### Cosmic Ray Exposure Ages

The production rates of cosmogenic <sup>3</sup>He, <sup>21</sup>Ne, and <sup>38</sup>Ar derived from the model for OCs from Leya

and Masarik (2009) and the resulting CRE ages are given in Table 8. The cosmogenic <sup>3</sup>He, <sup>21</sup>Ne, and <sup>38</sup>Ar concentrations used to calculate the CRE ages were error-weighted averages of the values for both aliquots. While

TABLE 6. Nucleosynthetic Ti and Cr isotope data of Elmshorn.

Sample	$n$ (Ti) <sup>a</sup>	$\epsilon^{46}\text{Ti}$	2 SE <sup>b</sup>	$\epsilon^{48}\text{Ti}$	2 SE <sup>b</sup>	$\epsilon^{50}\text{Ti}$	2 SE <sup>b</sup>	$n$ (Cr) <sup>a</sup>	$\epsilon^{53}\text{Cr}$	2 SE <sup>b</sup>	$\epsilon^{54}\text{Cr}$	2 SE <sup>b</sup>
Elmshorn	10	-0.09	0.09	-0.02	0.05	-0.53	0.06	6	0.23	0.10	-0.30	0.15
Forest Vale <sup>c</sup>	9	-0.16	0.05	-0.06	0.03	-0.57	0.07					
BHVO-2	8	0.00	0.09	0.01	0.04	0.06	0.05					
DTS-2								8	0.03	0.05	0.06	0.10

<sup>a</sup>Number of measurements.

<sup>b</sup>Isotopic values are averages of repeats. Uncertainties are given in 2 SE (SE = SD/ $\sqrt{n}$ ).

<sup>c</sup>Titanium analysis by Williams (2015), remeasured in this study.

the  $^{21}\text{Ne}_{\text{cos}}$  ( $T_{21}$ ) and  $^{38}\text{Ar}_{\text{cos}}$  ( $T_{38}$ ) ages overlap within their ranges, the  $^3\text{He}_{\text{cos}}$  ( $T_3$ ) age is significantly shorter. The lower age could be explained by a  $^3\text{He}$  loss due to heating (e.g., during atmospheric entry), which preferentially affects the lighter noble gases. Comparing the  $(^3\text{He}/^{21}\text{Ne})_{\text{cos}}$  and  $(^{22}\text{Ne}/^{21}\text{Ne})_{\text{cos}}$  ratios for Elmshorn 1 and 2 with the study from Nishiizumi et al. (1980), however, does not show a sufficiently large  $^3\text{He}$  loss. Alternatively, or additionally, it could also result from an overestimation of the  $^3\text{He}$  production rate in the Leya model. Dalcher et al. (2013) compared the  $(^3\text{He}/^{21}\text{Ne})_{\text{cos}}$  and  $(^{22}\text{Ne}/^{21}\text{Ne})_{\text{cos}}$  predicted by the Leya model with data collected from 138 chondrites in Nishiizumi et al. (1980), and the study showed systematically higher  $^3\text{He}_{\text{cos}}$  values for the Leya model. An overestimated production rate would mean that less time would have been needed to produce our measured  $^3\text{He}_{\text{cos}}$ , leading to an underestimation of the CRE age. The difference in  $(^3\text{He}/^{21}\text{Ne})_{\text{cos}}$  between the average trends suggested by the observed and model data (see figure 1 from Dalcher et al., 2013) at  $(^{22}\text{Ne}/^{21}\text{Ne})_{\text{cos}} \sim 1.111$  (measured for Elmshorn) would be about 15%, as estimated from the averaged lines. This suggests that perhaps both the overestimated production rate and some loss of  $^3\text{He}_{\text{cos}}$  could have contributed to the low  $T_3$ . Our preferred CRE age for Elmshorn is  $\sim 17$ –20 Myr.

### Further Constraints on Preatmospheric Radius and Shielding Depths by Cosmogenic Radionuclides

The IAMS determined nuclide ratios, which can be explained by long CRE ages (resulting in saturation of the respective radionuclide), that is, around  $10^{-10}$  and  $10^{-12}$  for  $^{26}\text{Al}/^{27}\text{Al}$  and  $^{41}\text{Ca}/^{40}\text{Ca}$  (Table 9), respectively. Associated machine blanks were 3–4 orders of magnitude lower, hence, no blank correction was applied to the results. Due to missing uncertainties for the used stable Al and Ca concentrations, no further uncertainty was added to specific activities. As IAMS samples (containing only about 1% Al and Ca each) are generally resulting in lower stable nuclide currents than those from chemically processed  $\text{Al}_2\text{O}_3$  and  $\text{CaF}_2$  samples (1%–2%), the counting statistics show low results.

The  $^{26}\text{Al}$  value from IAMS (originating from a 0.6 g aliquot of E03) is in reasonable (2-sigma) agreement with the  $^{26}\text{Al}$  value from gamma spectrometry (originating from the 233.5 g large E02), which can be well-explained by the inhomogeneous and thus perhaps different chemical compositions, that is, target element concentrations for production of  $^{26}\text{Al}$ , in the two specimens. The IAMS  $^{26}\text{Al}$  value agrees within 1-sigma with the  $^{26}\text{Al}$  gamma spectrometric value of E01, not only due to the much higher relative uncertainty of E01 compared to E02. The comparison (Figure 14) of the experimental  $^{26}\text{Al}$  and  $^{41}\text{Ca}$  with radius- and depth-dependent (saturation) production rate calculations (Leya & Masarik, 2009) let us further constrain the radius to 20–40 cm and a near-surface sample origin of E03 in the meteoroid. Both nuclide concentrations clearly exclude larger radii, hence, confirming the determination of a radius between 25 and 50 cm and low shielding of 6–10 cm based on the noble gas data and ablation considerations above. Updated Monte Carlo-calculated production rates, especially for  $^{41}\text{Ca}$  would be highly appreciated, but are not yet at our disposal. A more recent value for the half-life of  $^{41}\text{Ca}$  (Jörg et al., 2012) and the need for renormalization of underlying thin- and thick-target cross-section measurements to at-that-time used  $^{41}\text{Ca}/\text{Ca}$  standards (Geppert et al., 2005) should increase the accuracy of the calculated production rates resulting in better size and shielding information for meteorite samples.

The gamma-measured specific activity of  $^{22}\text{Na}$  of Elmshorn (E02) compared to radius- and depth-dependent (saturation) production rate calculations for  $^{22}\text{Na}$  (Leya et al., 2021, Figure S7) can be explained by a preatmospheric rather near-surface exposure within a body of smaller radii ( $>12.5$  cm), too. However, the measured  $^{22}\text{Na}$  alone is generally compatible with radii up to 80 cm.

### U/Th-He and K-Ar Gas Retention Ages

The U/Th-He ( $T_4$ ) and K-Ar ( $T_{40}$ ) chronometers for both Elmshorn 1 and 2 yield comparable gas retention ages (Table 10). The similarity in both systems - although

TABLE 7. Noble gas concentrations and isotope ratios in Elmshorn (sample E03).

(a) Helium and Ne concentrations (in $10^{-8} \text{ cm}^3 \text{ STP g}^{-1}$ ) and isotopic ratios							
Sample	Mass (mg)	$^4\text{He}$	$^3\text{He}/^4\text{He} \times 10^4$	$^{20}\text{Ne}$	$^{20}\text{Ne}/^{22}\text{Ne}$	$^{21}\text{Ne}/^{22}\text{Ne}$	$^{22}\text{Ne}/^{21}\text{Ne}$
Elmshorn 1	$15.307 \pm 0.023$	$882.4 \pm 3.1$	$214.2 \pm 2.3$	$5.095 \pm 0.027$	$0.8644 \pm 0.0035$	$0.9035 \pm 0.0040$	$1.1068 \pm 0.0049$
Elmshorn 2	$15.090 \pm 0.026$	$888.1 \pm 3.3$	$210.8 \pm 1.2$	$5.190 \pm 0.037$	$0.8704 \pm 0.0048$	$0.8950 \pm 0.0047$	$1.1173 \pm 0.0058$
Mean						$0.8999 \pm 0.0030$	$1.1112 \pm 0.0038$

(b) Argon (in $10^{-8} \text{ cm}^3 \text{ STP g}^{-1}$ ) and Kr (in $10^{-10} \text{ cm}^3 \text{ STP g}^{-1}$ ) concentrations and isotopic ratios								
Sample	$^{36}\text{Ar}$	$^{40}\text{Ar}/^{36}\text{Ar}$	$^{84}\text{Kr}$	$^{78}\text{Kr}/^{84}\text{Kr}$	$^{80}\text{Kr}/^{84}\text{Kr}$	$^{82}\text{Kr}/^{84}\text{Kr}$	$^{83}\text{Kr}/^{84}\text{Kr}$	$^{86}\text{Kr}/^{84}\text{Kr}$
Elmshorn 1	$7.716 \pm 0.050$	$3.498 \pm 0.022$	$440.8 \pm 4.3$	$0.665 \pm 0.029$	$4.349 \pm 0.070$	$20.71 \pm 0.18$	$20.48 \pm 0.15$	$31.17 \pm 0.28$
Elmshorn 2	$7.439 \pm 0.038$	$3.458 \pm 0.017$	$441.2 \pm 4.1$	$0.631 \pm 0.033$	$4.345 \pm 0.082$	$20.74 \pm 0.17$	$20.91 \pm 0.40$	$30.42 \pm 0.30$
								$^{84}\text{Kr}=100$

(c) Xenon concentrations (in $10^{-10} \text{ cm}^3 \text{ STP g}^{-1}$ ) and isotopic ratios									
Sample	$^{132}\text{Xe}$	$^{124}\text{Xe}/^{132}\text{Xe}$	$^{126}\text{Xe}/^{132}\text{Xe}$	$^{128}\text{Xe}/^{132}\text{Xe}$	$^{129}\text{Xe}/^{132}\text{Xe}$	$^{130}\text{Xe}/^{132}\text{Xe}$	$^{131}\text{Xe}/^{132}\text{Xe}$	$^{134}\text{Xe}/^{132}\text{Xe}$	$^{136}\text{Xe}/^{132}\text{Xe}$
Elmshorn 1	$10.991 \pm 0.048$	$0.481 \pm 0.016$	$0.4039 \pm 0.0044$	$8.191 \pm 0.074$	$160.66 \pm 0.91$	$16.77 \pm 0.18$	$82.40 \pm 0.52$	$38.10 \pm 0.37$	$32.23 \pm 0.33$
Elmshorn 2	$10.205 \pm 0.058$	$0.519 \pm 0.026$	$0.402 \pm 0.017$	$8.227 \pm 0.064$	$158.35 \pm 0.97$	$16.18 \pm 0.16$	$80.89 \pm 0.56$	$37.20 \pm 0.31$	$30.91 \pm 0.29$
									$^{132}\text{Xe}=100$

TABLE 8. Suitable shielding conditions matching our measured  $(^{22}\text{Ne}/^{21}\text{Ne})_{\text{cos}}$  value, determined with the model by Leya and Masarik (2009) for H chondrite meteoroids adapted to Elmshorn sample E03, cosmogenic  $^3\text{He}$ ,  $^{21}\text{Ne}$ , and  $^{38}\text{Ar}$  isotope concentrations (in  $10^{-8}\text{ cm}^3\text{ STP g}^{-1}$ ), production rates  $P_x$  (in  $10^{-8}\text{ cm}^3/[\text{g} \times \text{Myr}]$ ) and CRE ages  $T_x$  (Myr).

Sample	Preatmospheric radius (cm) <sup>a</sup>	Sample depth within meteoroid (cm)	$^3\text{He}_{\text{cos}}$	$^{21}\text{Ne}_{\text{cos}}$	$^{38}\text{Ar}_{\text{cos}}$
Elmshorn 1			$18.90 \pm 0.19$	$5.325 \pm 0.029$	$0.863 \pm 0.021$
Elmshorn 2			$18.721 \pm 0.086$	$5.337 \pm 0.037$	$0.860 \pm 0.017$
Mean	25–50	6–10	$18.752 \pm 0.079$	$5.330 \pm 0.023$	$0.861 \pm 0.013$

Sample	$P_3$	$P_{21}$	$P_{38}$	$T_3$	$T_{21}$	$T_{38}$	Preferred age
Elmshorn 1							
Elmshorn 2							
Mean	1.63–1.72	0.30–0.32	0.044–0.047	~11–12	~17–18	~18–20	~17–20

<sup>a</sup>See text for constraint of upper limit.

TABLE 9. Nuclide ratios measured by IAMS and resulting specific radionuclide activities in Elmshorn.

	$^{26}\text{Al}/^{27}\text{Al}$	$^{26}\text{Al}$ (dpm $\text{kg}^{-1}$ )	$^{41}\text{Ca}/^{40}\text{Ca}$	$^{41}\text{Ca}$ (dpm $\text{kg}^{-1}$ )
Elmshorn	$(1.110 \pm 0.036) \times 10^{-10}$	$52.4 \pm 1.7$	$(4.90 \pm 0.72) \times 10^{-12}$	$9.8 \pm 1.4$
Blank	$(6.4 \pm 2.4) \times 10^{-14}$		$(2.8 \pm 2.8) \times 10^{-15}$	

TABLE 10. Radiogenic  $^4\text{He}$  and  $^{40}\text{Ar}$  concentrations (in  $10^{-8}\text{ cm}^3\text{ STP g}^{-1}$ ), K concentrations (ppm), U and Th concentrations (ppb) measured on the ICP-SFMS (Table 5), and U/Th-He and K-Ar chronometer-derived gas retention ages  $T_x$  (Gyr).

Sample	$^4\text{He}_{\text{rad}}$	$^{40}\text{Ar}_{\text{rad}}$	K	U	Th	$T_4$	$T_{40}$
Elmshorn 1	$775.6 \pm 9.1$	$2343 \pm 18$					
Elmshorn 2	$782.4 \pm 9.0$	$2265 \pm 15$					
Average	$779 \pm 12$	$2306 \pm 56$	997	9	36	2.88–2.95	2.60–2.67

He is more volatile than Ar - suggests that no major resetting events occurred since  $\sim 2.8$  Gyr. The age recorded could potentially represent the closure time after the catastrophic collision between H and L chondrite parent bodies and re-accretion of Elmshorn's parent body. The only slightly higher  $T_4$  age (2.88–2.95 Gyr) relative to the  $T_{40}$  age (2.60–2.67 Gyr) could be due to chemical heterogeneities within Elmshorn. For example, assuming a deviation of  $\pm 10\%$  of the measured U, Th, and K concentrations would lead to an overlap between the  $T_4$  (2.68–3.19 Gyr) and  $T_{40}$  (2.47–2.82 Gyr) ages.

### Further Short- and Long-Lived Radionuclides by Gamma Spectrometry

For Elmshorn samples E01 and E02, the gamma lines were detected from members of the natural decay series of the primordial nuclides  $^{238}\text{U}$  and  $^{232}\text{Th}$  as well as of  $^{40}\text{K}$

(Table 11) and short-lived cosmogenic nuclides. A total number of 12 cosmogenic radionuclides were detected above the decision thresholds of the method. Their half-lives range from 5.6 days ( $^{52}\text{Mn}$ ) up to 705,000 years ( $^{26}\text{Al}$ ).

The radionuclide data (Table 11) do not allow any statement about possible disequilibria in the decay series. However, assuming an equilibrium state of the decay series, the terrestrial isotope ratios, and a homogenous distribution in each sample, the U, Th, and K concentrations of the sample E01 would be  $18.5 \pm 2.2\text{ ng g}^{-1}$ ,  $42 \pm 4\text{ ng g}^{-1}$ , and  $910 \pm 120\text{ }\mu\text{g g}^{-1}$ , respectively. For sample E02, U, Th, and K concentrations of  $11.4 \pm 1.3\text{ ng g}^{-1}$ ,  $47 \pm 4\text{ ng g}^{-1}$ , and  $750 \pm 60\text{ }\mu\text{g g}^{-1}$ , respectively, were calculated. The values of both samples slightly differ from each other and compared with bulk compositional data obtained from Elmshorn fragment E03 (Table 5) showing the heterogeneity of the entire body.

TABLE 11. Specific activities of radionuclides determined by gamma spectrometry. All activity data are referenced to the date of the respective falls, i.e., September 12, 2019 (Flensburg) and April 25, 2023 (Elmshorn: stones E01 and E02). Half-lives are from the Decay Data Evaluation Project (DDEP, 2023) or for  $^{26}\text{Al}$  from Norris et al. (1983). Data about the German fall Flensburg, which occurred in close neighborhood, are included for comparison (Bischoff et al., 2021).

Radionuclide	Half-life	Specific activity (dpm kg <sup>-1</sup> ) Flensburg	$\sigma$ (%)	Specific activity (dpm kg <sup>-1</sup> ) Elmshorn (E01)	$\sigma$ (%)	Specific activity (dpm kg <sup>-1</sup> ) Elmshorn (E02)	$\sigma$ (%)
<i>Cosmogenic</i>							
$^7\text{Be}$	53.22 days	121	14	<b>86</b>	20	<b>89</b>	11
$^{22}\text{Na}$	2.6029 years	65	8.8	<b>109</b>	13	<b>90</b>	8.1
$^{26}\text{Al}$	$7.05 \cdot 10^5$ years	<1.7		<b>56</b>	12	<b>46</b>	8.4
$^{46}\text{Sc}$	83.787 days	12.6	13	<b>10.7</b>	15	<b>11.1</b>	10
$^{44}\text{Ti}^a$	60.0 years	n.a.		<b>1.1</b>	26	< <b>1.7</b>	
$^{48}\text{V}$	15.9735 days	26	17			<b>21.8</b>	9.6
$^{51}\text{Cr}$	27.704 days	116	21			<b>95</b>	12
$^{52}\text{Mn}$	5.592 days	n.a.				<b>20</b>	15
$^{54}\text{Mn}$	312.19 days	150	8.0	<b>145</b>	12	<b>176</b>	7.8
$^{56}\text{Co}$	77.236 days	7.3	19	<b>8.4</b>	15	<b>7.1</b>	11
$^{57}\text{Co}$	271.81 days	13.5	13	<b>18.5</b>	12	<b>15.3</b>	8.5
$^{58}\text{Co}$	70.85 days	16.4	13	<b>12.2</b>	15	<b>16.5</b>	9.0
$^{60}\text{Co}$	5.2711 years	98	8.1	<b>2.9</b>	15	<b>4.3</b>	11
<i>Primordial and decay series</i>							
$^{238}\text{U}$ decay series							
$^{238}\text{U}$	$4.468 \cdot 10^9$ years	<22		< <b>35</b>		< <b>60</b>	
$^{226}\text{Ra}$	1600 years	13.3	11	<b>13.7</b>	12	<b>8.4</b>	11
$^{210}\text{Pb}$	22.23 years	<27		< <b>78</b>		< <b>110</b>	
$^{232}\text{Th}$ decay series							
$^{228}\text{Ra}$	5.75 years	<24	15	<b>10.4</b>	15	<b>12.4</b>	15
$^{228}\text{Th}$	1.9126 years	16.6	13	<b>10.2</b>	11	<b>11.2</b>	10
$^{40}\text{K}$	$1.2504 \cdot 10^9$ years	780	8.1	<b>1680</b>	13	<b>1400</b>	8.1

Note: Bold indicates the actual measured values.

Abbreviation: n.a., not analyzed.

<sup>a</sup>An equilibrium between  $^{44}\text{T}$  and  $^{44}\text{Sc}$  was assumed.

TABLE 12. Data about the saturation magnetization ( $M_s$ ) and magnetic susceptibility ( $\log \chi$ ) of different aliquots of the Elmshorn stones E03 and E07 analyzed at CEREGE. Analytical errors are negligible. For comparison data for H and L chondrites are given: (1)  $M_s$  average values from Gattacceca et al. (2014); (2)  $\log \chi$  average values from Rochette et al. (2003).

Stones	Sample type	Mass (mg)	$M_s$ (Am <sup>2</sup> kg <sup>-1</sup> )	Log $\chi$	Similar to:
Elmshorn E03	(a) H6-fragment	238	32.4	5.30	H chondrites (1, 2)
Elmshorn E03	(b) Main lithology	267	40.0	5.10	H chondrites (1, 2)
Elmshorn E07	(c) Main lithology	427	20.4	5.01	L chondrites (1, 2)
E07—c1	Subsample	277	15.4	5.05	L chondrites (1, 2)
E07—c2	Subsample	150	29.6	4.93	L chondrites (1, 2)
H chondrites	Mean of falls (1,2)	Bulk	40.46	5.32	
L chondrites	Mean of falls (1,2)	Bulk	17.93	4.87	

### Micro-Fourier Transform Infrared Spectroscopy

In order to study the spectroscopic characteristics of the rock, the three discernable lithologies from E03

(Figure 4c) were separately analyzed by micro-Fourier transform infrared ( $\mu$ -FT-IR) spectroscopy. All three show a dominantly crystalline spectrum in the investigated areas. The dark fine-grained groundmass (related to the

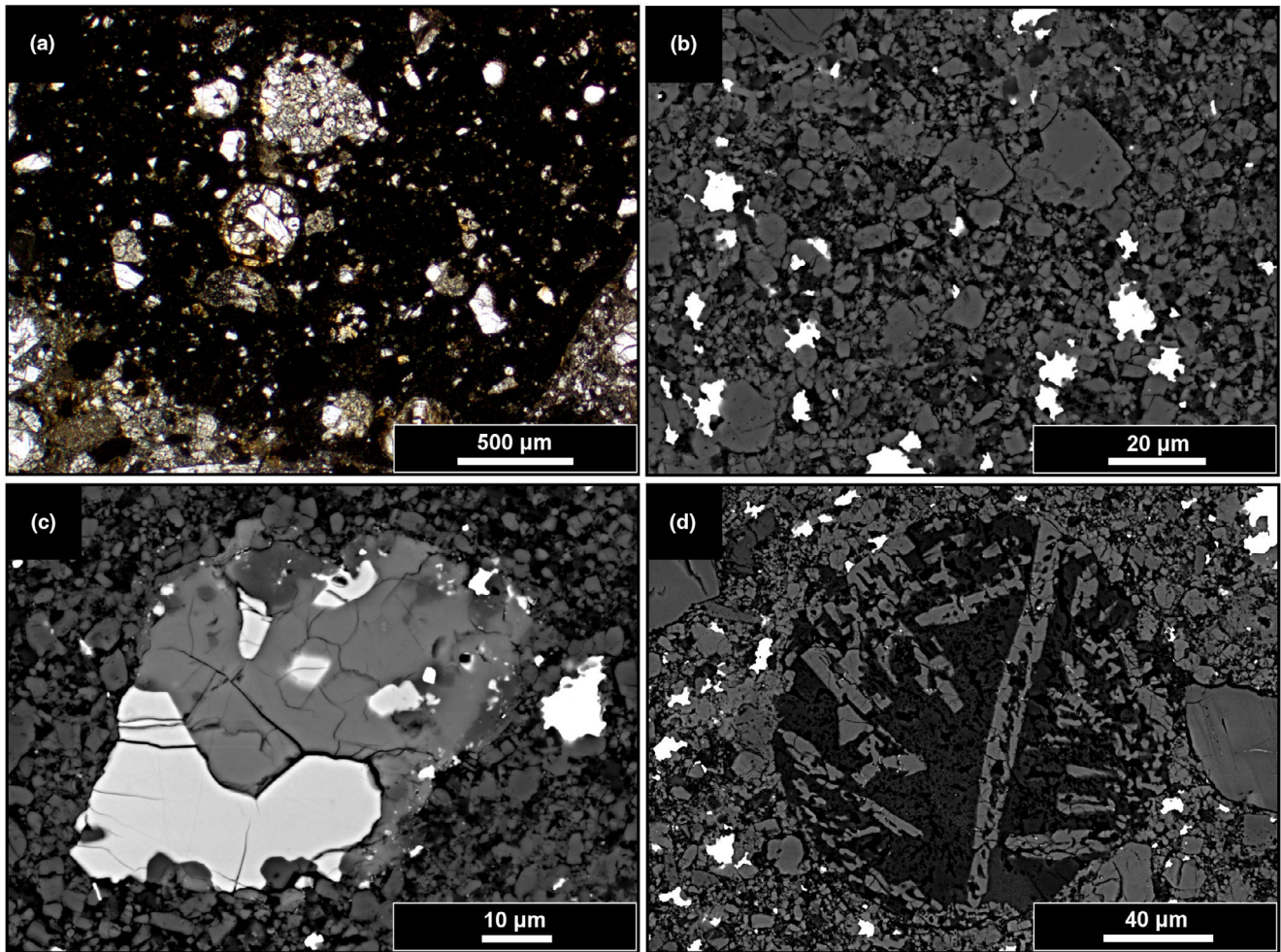


FIGURE 7. (a) Part of a dark fragment from E03 ( $\sim 0.5$  cm in apparent size) containing several chondrules and chondrule fragments. The clast has a sharp boundary to the brecciated main portion of the rock (plane polarized light). (b) Area within the dark lithology. Small irregularly shaped metal grains (white) are homogeneously distributed and probably responsible for the dark appearance (BSE image). (c) Phosphate (gray)–chromite (light gray) paragenesis (BSE image). (d) Al-rich relict chondrule within the dark lithology; skeletal olivines embedded in a crystalline Na,Al-rich groundmass (BSE image).

dark clast in Figure 4a) and the bulk mass of the light clast (Figure 4b) both display olivine-dominated spectra. The olivine observed in the light lithology shows bands consistent with a high Fo portion at 1030, 971, 923, 893, 833, and 620  $\text{cm}^{-1}$ . The finer grained groundmass of the dark lithology shows rather attenuated Reststrahlen and combination bands at 1003, 973<sup>1</sup>, 886, and 832  $\text{cm}^{-1}$  with additional, rather less defined peaks between 952 and 900  $\text{cm}^{-1}$ . The finer grained dominating lithology (the clastic groundmass: medium-light: Figure 4c) appears to be dominated by a low-Ca pyroxene and shows additional Reststrahlen bands (RB; i.e., RBs are reflectance maxima that are mineral diagnostic) at 724, 685, and 644  $\text{cm}^{-1}$ . Mineral diagnostic spectral features, for example, the Christiansen feature (CF), or the mineral diagnostic RBs are indicated in Figure 15 as CF and black arrows. The

CF alternates between 1140 and 1135  $\text{cm}^{-1}$  in the bulk measurements.

### Density Measurements

Published values for the densities of H chondrites and L chondrites are  $3.42 \pm 0.18 \text{ g cm}^{-3}$  and  $3.36 \pm 0.16 \text{ g cm}^{-3}$ , respectively (Consolmagno et al., 2008). The density of several Elmshorn fragments were measured. The volume of one piece (E02) of  $233.5 \pm 0.1 \text{ g}$  was obtained by two techniques: first, by a method described by Consolmagno et al. (2008) and, second, by CT procedures. The first type of measurement led to a volume of  $70.0 \pm 1.0 \text{ cm}^3$  ( $n = 13$ ) and a density ( $\rho$ ) of  $3.34 \pm 0.05 \text{ g cm}^{-3}$ . For the same 233.5 g piece, the high-precision CT technique led to a volume of  $69.73 \text{ cm}^3$  and a

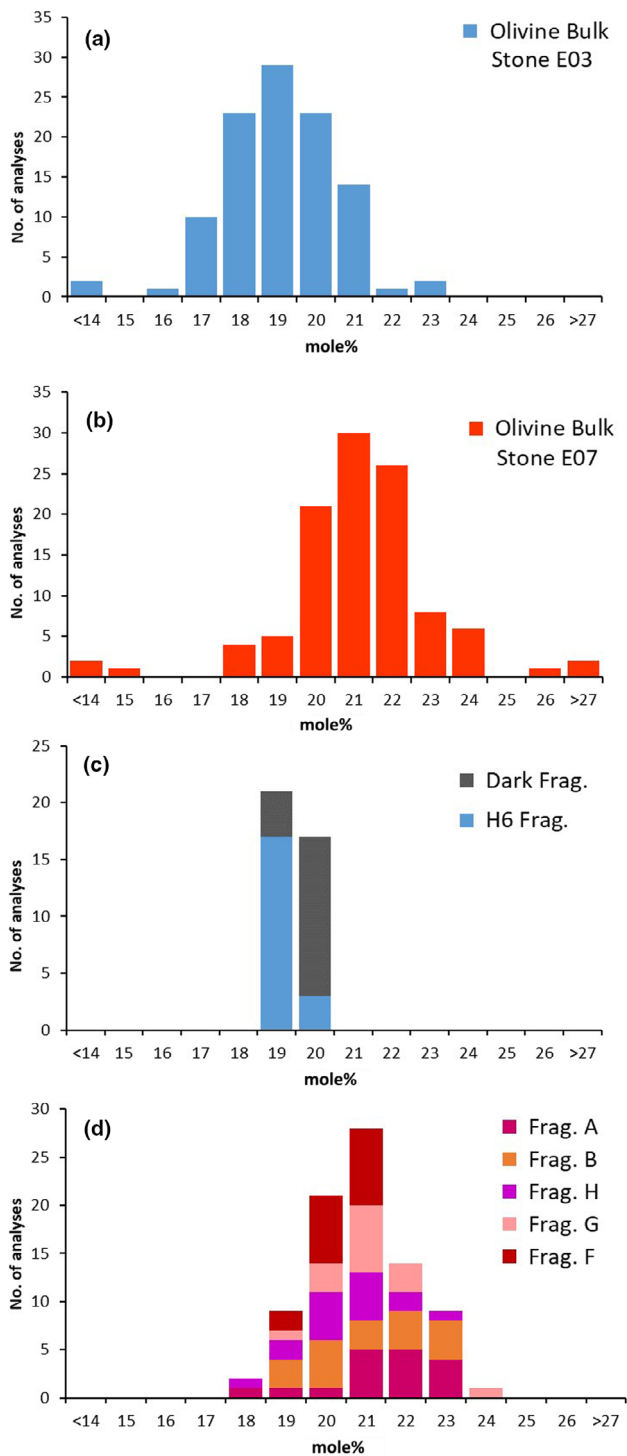


FIGURE 8. Olivine compositions (Fa in mole%): (a) of bulk sample of E03; (b) of bulk sample of E07; (c) olivine compositions of the H6 and dark fragment (see Figure 4; E03); (d) olivine compositions of five type H/L or L3.9-4 fragments from E03. Chemical details are given in Table 1.

density ( $\rho$ ) of  $3.349 \pm 0.010 \text{ g cm}^{-3}$ . Thus, both values are similar (mean:  $3.344 \text{ g cm}^{-3}$ ). Using the CT technique, the volume of a second piece from a different individual object (E03) from the meteorite strewn field of 51.62 g was obtained and found to be  $14.97 \text{ cm}^3$ . These data lead to a density of  $3.448 \pm 0.010 \text{ g cm}^{-3}$ . By digital optical techniques, the volume of the largest piece (E01) was found to be  $1119.105 \text{ cm}^3$ . Considering its mass of 3731 g, a density of  $3.334 \pm 0.003 \text{ g cm}^{-3}$  is calculated. Thus, two stones have densities of about  $3.34 \text{ g cm}^{-3}$ , while the third one has a significantly higher density of  $3.45 \text{ g cm}^{-3}$ .

Considering the obtained density values, the E03 fragment has a similar value to that of mean H chondrites, whereas the pieces of E01 and E02 have similar densities to those obtained for mean L chondrites.

### Magnetic Susceptibility

The (MS) of different fragments of the Elmshorn breccia analyzed in Nördlingen indicate a wide range of values (Table S3). The weighted overall mean value of  $\log \chi = 5.07 \pm 0.03$  (with  $\chi$  in  $10^{-9} \text{ m}^3 \text{ kg}^{-1}$ ) is in between the average values of  $4.87 \pm 0.10$  and  $5.32 \pm 0.10$  for falls of L and H chondrites, respectively (Rochette et al., 2003). Large samples ( $> \sim 10 \text{ g}$ ) including the main mass plot within a kind of transition zone between H and L chondrites. The values for small samples scatter in a wide range around the average with a majority tending toward L and only few ones to H chondrite lithologies. Similarly, the values for the MS of different aliquots from E03 cover a large field between the mean values for H and L chondrites (Figure 16). The scattering indicates inhomogeneities in the distribution of ferromagnetic metal on a scale of centimeters to millimeters and corresponds to a range of roughly 7–13 wt%.

Two samples from the E03 fragment without fusion crust were studied at CEREGE: a 267 mg bulk slice and a 238 mg fragment of type 6 lithology (Table 12). The two samples gave similar results and were aggregated. The mean MS  $\log \chi = 5.21$  (where  $\chi$  is in  $10^{-9} \text{ m}^3 \text{ kg}^{-1}$ ; analytical errors are negligible) is within the expected range for an H chondrite fall ( $5.32 \pm 0.10$ ,  $n = 144$ ; Rochette et al., 2003). Saturation magnetization  $M_S = 37.1 \text{ Am}^2 \text{ kg}^{-1}$  is also within the expected range for H chondrite falls ( $40.46 \pm 6.99 \text{ Am}^2 \text{ kg}^{-1}$ ;  $n = 25$ ; Gattacceca et al., 2014). The 437 mg sample from stone E07, which was selected based on the low  $\log \chi$  values (Figure 16) for comparison, clearly shows different results. The Ms value, which is the best proxy for the metal abundance, is close to that of L chondrite falls (Table 12:  $17.93 \pm 6.09$ ;  $n = 31$ ; Gattacceca et al., 2014).



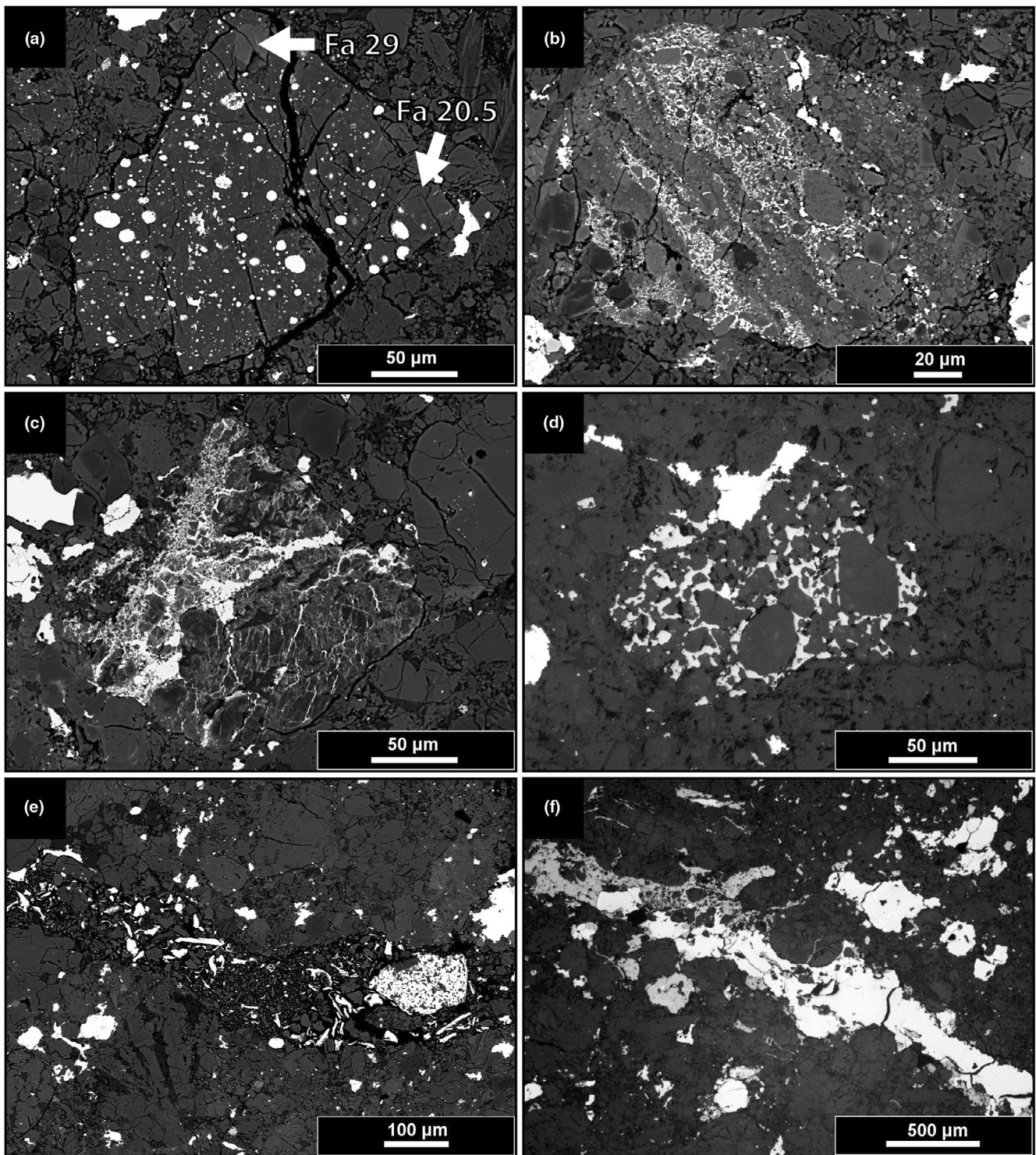


FIGURE 9. (a) Fragment of an impact melt lithology with metal–sulfide spherules and some relict olivines clasts of  $Fa_{29}$  and  $Fa_{20.5}$  (BSE image); (b) fragment containing veins like features rich in metals and sulfides that probably formed by shock (BSE image); (c) shock-darkened fragments with metals and sulfides coating all fractures and spaces of the silicates (BSE image); (d) sulfides embedding silicate clasts (reflected light); (e) porous vein-like area with metals (often Ni-poor [ $\sim 2$  wt%]) and sulfides of unusual morphology (BSE image); (f) several millimeter-sized, vein-like metal–sulfide associations (reflected light). All images from sample E03.

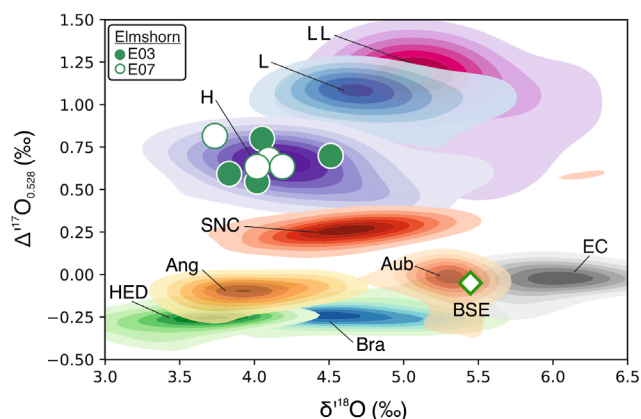


FIGURE 10. Triple oxygen isotope compositions ( $\Delta^{17}\text{O}$  vs.  $\delta^{18}\text{O}$ ) of eight individual chips ( $\sim 2\text{ mg}$  each) from two different fragments of Elmsborn (E03, E07) in comparison with the compositions of ordinary chondrites (H, L, LL) and other noncarbonaceous clan meteorites (Ang, angrites; Aub, aubrites; Bra, brachinites; EC, enstatite chondrites; HED, howardites, eucrites, diogenites; SNC, shergottites, nakhlites, chassignites) and the bulk silicate Earth (BSE). Meteorite reference compositions were compiled from the Meteoritical Bulletin Database and are shown with Kernel density estimation contours, with the outermost contours for a given meteorite group encompassing 70% of the corresponding data populations. The composition of the BSE was taken from Peters et al. (2021).

The MS ( $\log \chi$ ) gives more or less the same result but is less robust considering the metal abundance.

The hysteresis properties, with very low coercivity ( $B_C = 2.9\text{ mT}$ ), low  $M_{RS}/M_S$  ( $1.16 \times 10^{-2}$ ), and high  $B_{CR}/B_C$  (30.0) are typical of equilibrated H chondrites, with induced magnetic properties dominated by multidomain kamacite (Gattacceca et al., 2014). The  $S_{-300}$  value of 0.51 indicates the presence of significant high-coercivity ferromagnetic minerals that can be identified as tetraenaite in the cloudy zone structure (Gattacceca et al., 2014). The coercivity spectra derived from IRM acquisition for the two samples can be fitted with two components with coercivity peaks at 4.7 and 143 mT (238 mg sample), and 65 and 353 mT (267 mg sample). Although there is some significant intersample variability, the existence of a component with very high coercivity indicates that the tetraenaite in the cloudy zone microstructure is ordered.

The two Elmsborn samples from stone E03 have magnetic properties typical of equilibrated H chondrites. This result is expected for the H6 clast and shows that the second sample of the stone representing the fine-grained clastic main lithology is also dominated by H chondrite components. The magnetic properties show a rock with metal under the form of multidomain kamacite and remanence properties dominated by the cloudy zone

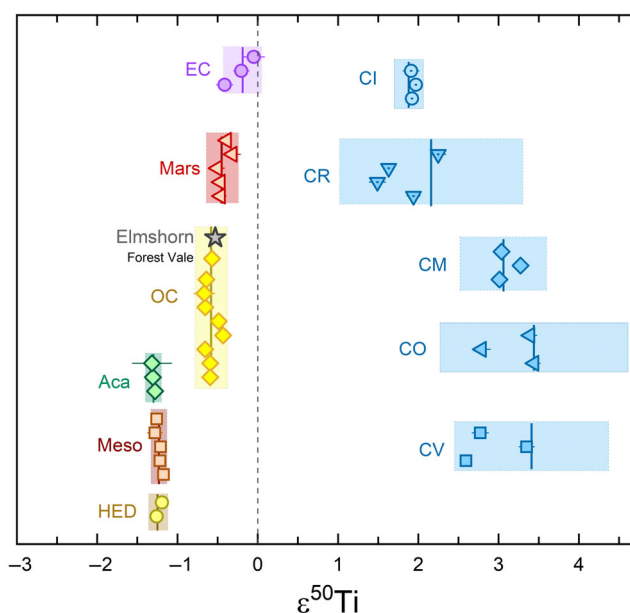


FIGURE 11. The Ti isotope composition of Elmsborn (gray star) is consistent with both the simultaneously analyzed OC Forest Vale and literature values of individual OCs (yellow symbols). The data reveal deficits in  $\epsilon^{46}\text{Ti}$  and  $\epsilon^{50}\text{Ti}$  relative to Earth, indicating their formation in the inner solar system, i.e., the NC (noncarbonaceous meteorite) reservoir. Colored fields represent averages of meteorite groups (line) with 2 SD uncertainty (envelope) based on literature data (for data compilation and references, see Rüfenacht et al., 2023). Individual data points represent bulk meteorite samples, which were analyzed in the same laboratory as Elmsborn at ETH Zurich and are published in Rüfenacht et al. (2023). Aca, acapulcoites; EC, enstatite chondrites; Meso, mesosiderites; OC, ordinary chondrites. Literature data of OCs are from Trinquier et al. (2009), Zhang et al. (2011, 2012), Williams (2015), Burkhardt et al. (2017), Bischoff et al. (2017), Bischoff, Barrat, et al. (2019), Gerber et al. (2017), Williams et al. (2021), and Rüfenacht et al. (2023). Figure adapted from Rüfenacht et al. (2023).

microstructure with high coercivity. This high coercivity indicates that the tetraenaite in the cloudy zone was not disordered by transient thermal events following its formation during parent body metamorphic cooling, indicating the absence of shock above shock level S3 (Dos Santos et al., 2015; Gattacceca et al., 2014).

The sample from stone E07 shows completely different magnetic properties. It can be characterized by significantly lower metal abundance and the values for magnetic properties are very close to those of L chondrites. However, it should be considered that on such small samples (Table 12) it is difficult to be definitive, because  $M_s$  depends on the relative abundance of kamacite, taenite, and tetraenaite (higher nickel leads to lower  $M_s$ ). Thus, a large kamacite grain or a large taenite grain can affect the result significantly.

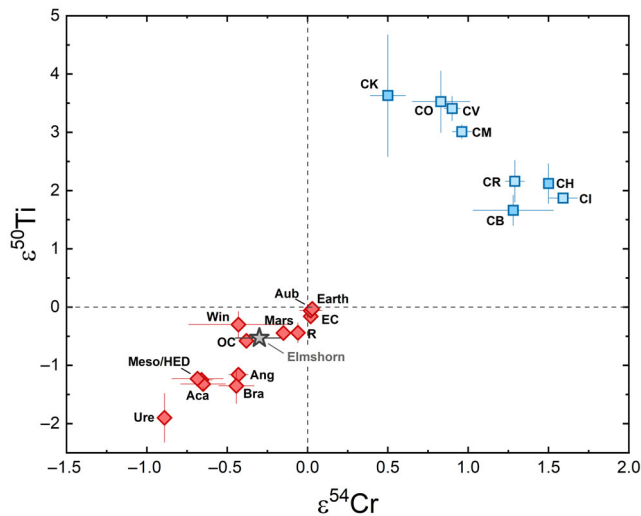


FIGURE 12. The Ti and Cr isotope compositions of Elmshorn (gray star) overlap with the group average of OCs within analytical uncertainty. Therefore, Elmshorn belongs to the category of noncarbonaceous chondrites, which are assumed to have formed from inner solar system material. The averages and corresponding uncertainties are taken from the compilation of Rüfenacht et al. (2023). Aca, acapulcoites; Ang, angrites; Aub, aubrites; Bra, brachinites; CC, carbonaceous chondrites; EC, enstatite chondrites; IAB sil, IAB silicates; Meso, mesosiderites; Win, winonaites.

## DISCUSSION

### General Aspects and the Significance of Radionuclide Concentrations from Gamma Spectrometry

From the recovered 21 fragments, most studies were done on sample E03, which hit the roof of a house and scattered into many fragments. Further studies for comparison were performed on sample E07. Nondestructive magnetic properties were obtained from most of the samples (Figure 16), whereas radionuclide concentrations were obtained from stones E01 and E02.

The short-lived radionuclides of the Elmshorn meteorite measured from May 4 until June 4, 2023, confirm the connection of the Elmshorn meteorite with the bolide event over Schleswig–Holstein (the state Elmshorn is located in) on April 25, 2023, since the presence of short-lived cosmogenic radionuclides with half-lives as short as 5.6 days proves the recent exposure to cosmic rays for both stones, the Elmshorn E02 (233.5 g) and the E01 (3731 g) stone (Table 11).

The U, Th, and K concentrations of the Elmshorn chondrite are in the same range as those found in gamma spectrometric studies of recent OC falls, like Stubenberg or Renchen (Bischoff et al., 2017; Bischoff, Barrat, et al., 2019). Compared to Flensburg, the U and Th values are similar, but Elmshorn shows a higher potassium content.

The short-lived cosmogenic radionuclides are also in the range of values measured for the Braunschweig, Stubenberg, or Renchen meteorites (Bartoschewitz et al., 2017; Bischoff et al., 2017; Bischoff, Barrat, et al., 2019). Flensburg also showed similar activities, except of  $^{60}\text{Co}$ : its distinctly higher value in Flensburg was explained by a larger depth of the fragment within the meteoroid (Bischoff et al., 2021).

### Classification of Elmshorn

Based on the inspection of the open surfaces (due to fragmentation) and the polished thin sections, the brecciated texture of Elmshorn is obvious (Figure 4). Within a dominating grayish clastic groundmass, large light- and dark-colored fragments can easily be recognized (Figure 4). Thus, Elmshorn is a breccia. Based on the randomly analyzed olivines and low-Ca pyroxenes, Elmshorn certainly contains unequilibrated type 3 lithologies. Strongly recrystallized and well-equilibrated type 6 clasts exist as well. Although some components (including glass-rich chondrules) are of low petrologic type 3, several lithologies were found that contain almost equilibrated (type 3.9–4.0) olivines but still have less equilibrated pyroxene. This behavior is often found in type 3.8–4 OCs, because the Fe–Mg exchange and, consequently, the equilibration of olivine is significantly faster than the Fe–Mg exchange in low-Ca pyroxene. Many of these type 3.9–4 lithologies with almost equilibrated olivine compositions point toward an intermediate H/L or L chondrite heritage (Figure 8). On the other hand, the light-colored type 6 fragment as well as many other constituents of the meteorite are clearly of H group origin, as shown in Figure 8, which represents the results of randomly obtained olivine compositions. Overall, we have an impact-produced mixture dominated by H and H/L (or L) chondrite lithologies.

The coexistence of components with H and L (or H/L) group characteristics is also suggested considering the results of the density and magnetic properties. Based on the densities obtained for the different pieces ( $3.334 \pm 0.003$  [E01],  $3.349 \pm 0.010$  [E02], and  $3.448 \pm 0.010 \text{ g cm}^{-3}$  [E03]) the clear difference is of diagnostic significance. Since the published values for H chondrites and L chondrites are  $3.42 \pm 0.18 \text{ g cm}^{-3}$  and  $3.36 \pm 0.16 \text{ g cm}^{-3}$ , respectively (Consolmagno et al., 2008), it appears that one of the three brecciated pieces from Elmshorn is dominated by H chondrite lithologies (the 51.62 g piece from E03) and the two other, larger ones by L chondritic components. The MS also confirms the results of the density analyses. Considering samples with mass above 3 g, the MS varies between  $\log \chi = 5.19 \pm 0.04$  and  $4.96 \pm 0.02$  (Figure 16, Table S3). Comparing values for falls of  $\log \chi = 5.32 \pm 0.10$  for H, and  $\log$

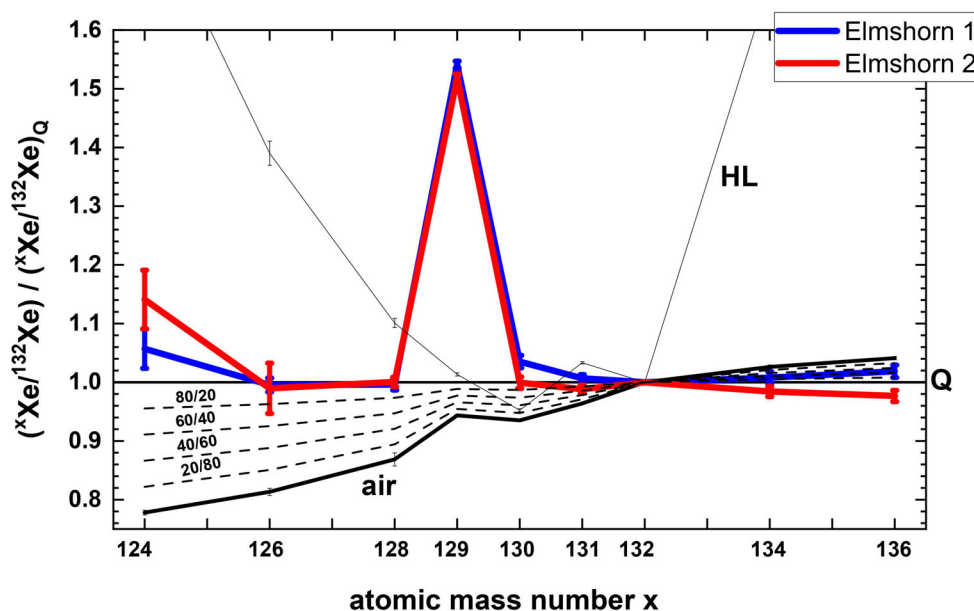


FIGURE 13. Xe isotopic compositions of Elmshorn 1 and 2 from stone E03 normalized to Xe-Q (Busemann et al., 2000). The dashed lines represent mixing lines of varying ratios between Q and air. The Xe-HL composition is taken from Huss and Lewis (1994), and the Xe-air from Basford et al. (1973). The Xe-trapped component is dominated by Q. A slight cosmogenic contribution ( $>1\sigma$ ) to  $^{124}\text{Xe}$  might be discernible, though this should typically affect  $^{126}\text{Xe}$  even more. Both samples show short-lived  $^{129}\text{I}$ -derived  $^{129}\text{Xe}$  excesses.

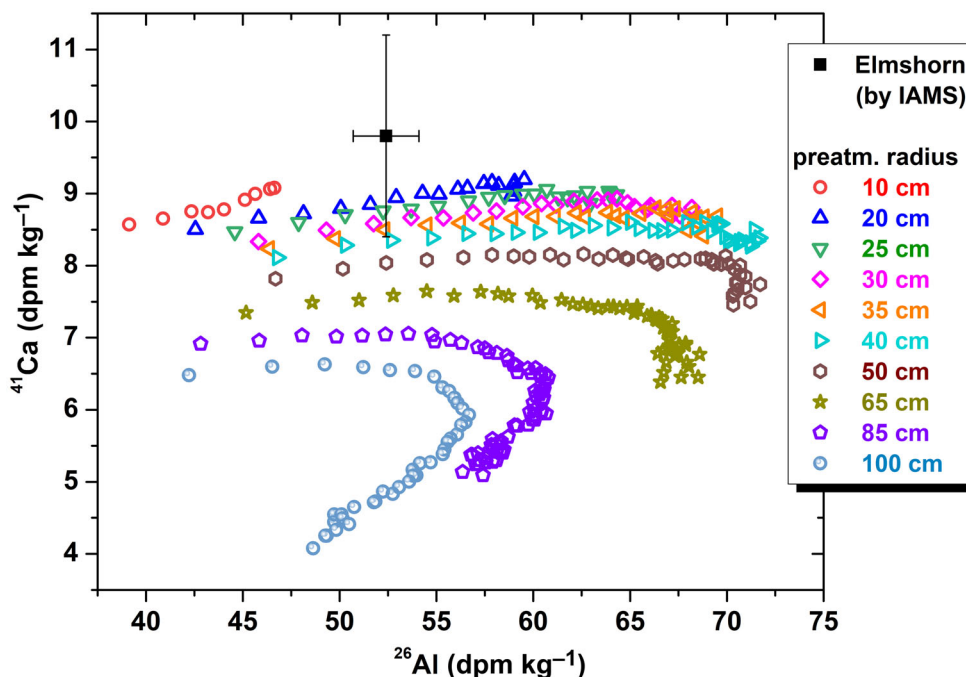


FIGURE 14. Specific activity of Elmshorn (black square) calculated from IAMS data with 1-sigma uncertainties compared to radius- and depth-dependent (saturation) production rate calculations for  $^{26}\text{Al}$  and  $^{41}\text{Ca}$  for OCs (Leya & Masarik, 2009). The production rates are based on the chemical composition in Table S2.

$\chi = 4.87 \pm 0.10$  for L (from Rochette et al., 2003), most of the Elmshorn stones look like being a mixture of H and L chondrite components. A similar conclusion is reached by

measuring the saturation magnetization of  $\sim 500$  mg samples. The obtained values of  $M_s = 36.5 \text{ Am}^2 \text{ kg}^{-1}$  for H-dominated and  $M_s = 20.4 \text{ Am}^2 \text{ kg}^{-1}$  for supposed L-

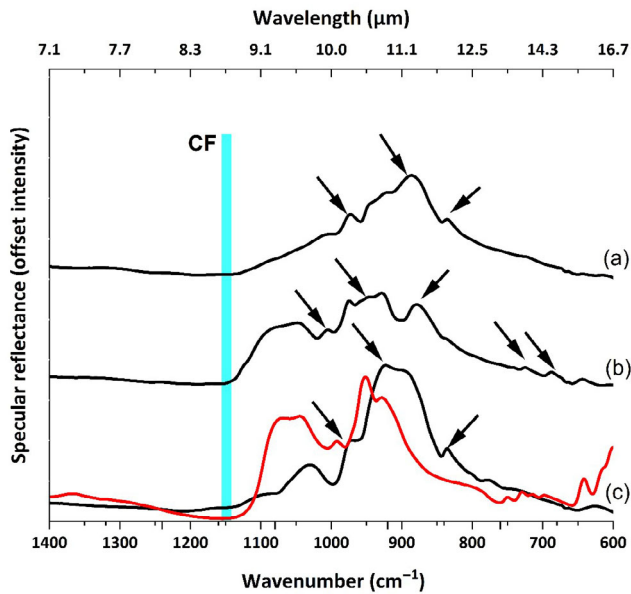


FIGURE 15. The three macroscopically distinct areas shown in Figure 4 (light and dark lithology from E03, as well as the dominating clastic groundmass [medium–light]) were identified in the thin section Elmshorn PL23029 and investigated by obtaining specular reflectance spectra of several designated areas of interest. Black arrows denote RBs typical for olivine (spectrum a) containing additional peaks (spectrum c), and albitic feldspar, and low-Ca pyroxene (spectrum b). The red spectrum is albite (ID167) (see database details in Weber et al. (2018) and inset for comparison of the RB positions). The position of the CF, which is a material-dependent reflectance minimum and indicated by a blue bar is in agreement with dominantly silicate-comprised material. (a) 609 Elmshorn PL 23029 dark lithology bulk spectrum; (b) 609 Elmshorn PL 23029 light coarse-grained bulk spectrum; (c) 609 Elmshorn PL 23029 medium–light multiclastic bulk spectrum. Spectra are offset for clarity. Depending on the abundance of metal and sulfide phases present in the measurement spot, several spectra show a general baseline enhancement (not visible here owing to offset).

dominated lithologies are very similar to values of  $40.46 \pm 6.99$  and  $17.93 \pm 6.09 \text{ Am}^2 \text{ kg}^{-1}$  for H and L chondrite falls, respectively (Gattacceca et al., 2014). The weighted overall mean value of  $\log \chi = 5.07 \pm 0.03$  is in between the average values of 4.87 and 5.32 for falls of L and H chondrites, respectively (Rochette et al., 2003). Assuming that Elmshorn represents a mix of such typical OC materials, the estimate yields an H chondrite contribution of about 30–40 wt%.

Consequently, Elmshorn can be described based on the chemical compositions of olivine and low-Ca pyroxene and density and magnetic considerations as an H-H/L (or H-L) breccia. Since we have clasts of different petrologic types (3–6), the bulk rock of Elmshorn could potentially be classified as an H-H/L3-6 or (H-L3-6) chondrite breccia. However, such a classification would

be inconsistent with the results of the O isotope analyses. All eight O isotope analyses from two different stones (one dominated by H chondrite lithologies, the other dominated by L chondrite lithologies) show typical values for H chondrites. Thus, the oxygen isotope compositions are unambiguous. They clearly indicate an H chondrite heritage even for those rocks that were characterized as H/L or L chondrites based on petrologic data (e.g., olivine compositions) and considerations concerning density and MS. In summary, Elmshorn shows extremely anomalous behavior. Taking the oxygen isotope composition as an accepted tool of classification into account, consequently, Elmshorn has to be classified as an “anomalous H3-6 chondrite breccia.” Titanium and Cr isotope analyses confirm that it is an OC.

As defined earlier for the shock classification of breccias, the fragment with the lowest degree of shock defines the shock degree of a brecciated bulk rock (Bischoff, Schleiting, et al., 2019; Stöffler et al., 1991, 2018). In many fragments, undulose extinction in olivine is the typical effect of shock metamorphism and unshocked fragments do not exist. Thus, an S2 (C-S2) shock classification for the Elmshorn breccia is appropriate.

### Formation of Elmshorn

As demonstrated earlier, Elmshorn contains various types of fragments that have seen various degrees of metamorphism and recrystallisation (Figure 5). This is well documented by the coexistence of type 5 or 6 fragments (Figure 5) and of fragments having glass-bearing chondrules with strongly zoned olivine ( $\text{Fa}_{0-27}$ ; Figure 6). Thus, Elmshorn clearly contains lithic components from the interior of the parent body(ies) as well as material from (near) surface locations. One type of material is of H chondrite heritage, as indicated by equilibrated lithologies having mean olivine compositions of  $\text{Fa}_{19-20}$  (Figure 8c). Another main component of Elmshorn can be described as an equilibrated (type 4) or almost equilibrated ( $\sim$ type 3.8–3.9) lithology with mean olivine compositions of  $\sim \text{Fa}_{21-23}$  (Figure 8d). Thus, the latter components have olivine compositions related to olivine in typical L chondrites ( $\sim \text{Fa}_{22-27}$ ). As such, Elmshorn consists of main components related to two independent precursor planetesimals. The coexistence of these two components is confirmed by the physical properties (density, MS) that indicate both an H and L (or H/L) chondrite relationship.

We suggest that the two parent bodies had already experienced shock processing, brecciation, and lithification prior to the disruption and re-accretion events that occurred possibly about 2.8 Gyr ago based on the gas retention ages (Table 10). This is indicated by the occurrence of several types of melt rocks (e.g., Figure 9a

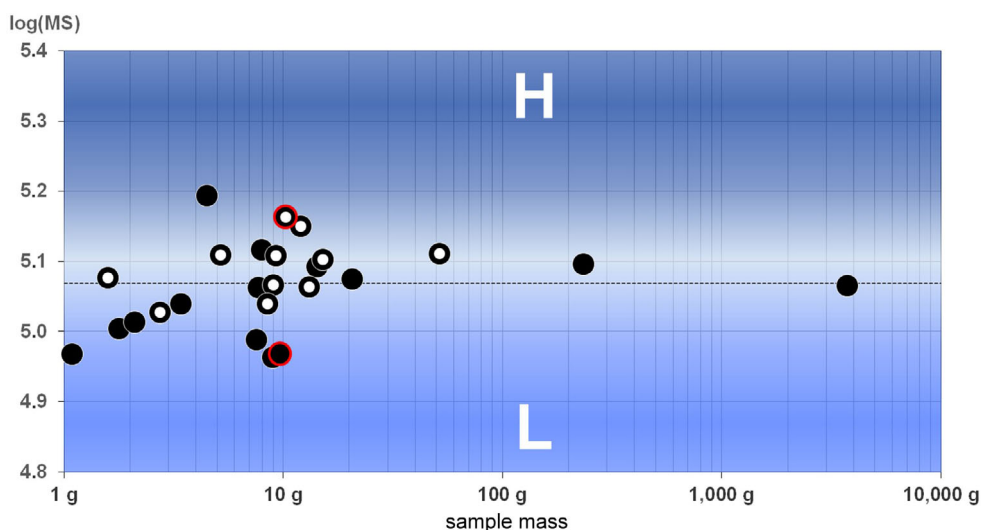


FIGURE 16. Illustration of the magnetic susceptibility (MS, in  $10^{-9} \text{ m}^3 \text{ kg}^{-1}$ ) of samples with different masses from Elmsborn shown as black points. The 11 measured fragments of the 156 g piece (E03; Tables S1 and S3) shattered on the roof of a house on “Gärtnerstrasse” are indicated by white centers. The two pieces studied in more detail in this work are highlighted by red outer circles. All data plot close to the transition zone between H and L chondrites. The average values of L and H chondrite falls are  $4.87 \pm 0.10$  and  $5.32 \pm 0.10$ , respectively (Rochette et al., 2003). The dashed line represents the weighted mean.

and Figure S4), some of which are certainly of impact origin. A typical example of an impact melt rock clast is shown in Figure 9a, illustrating the formation of immiscible metal–sulfide spherules in a silicate melt matrix. Based on its shape, this fragment must have been originally part of a larger melt unit. It remains unsolved, however, whether the fragment represents a piece of a former melt pool or melt vein. The occurrence of olivine fragments ( $\text{Fa}_{20}$ ,  $\text{Fa}_{29}$ ) may indicate that the melt formed within an unequilibrated part of the parent body, perhaps in a near-surface type 3 layer. Another strange melt rock (fragment M) is metal poor (Figure S4) with unusual Al-rich mafic silicates (Table 2). Other impact-related clasts are shown in Figure 9, including various types of shock-darkened clasts (Figure 9b,c) and sulfide–silicate associations (Figure 9d). Elmsborn contains even more unusual clasts that had to be part of larger units on a former parent body, and their formation and brecciation requires multiple impact processing steps. Since the brecciated main lithology of Elmsborn does not contain solar wind-implanted noble gases, the different components cannot have been part of a parent body regolith. Thus, Elmsborn is a fragmental breccia. The brecciated nature without the presence of solar wind is even more difficult to understand given that Elmsborn also frequently contains type 3 clasts with glass-rich chondrules (Figures 5 and 6) that may represent lithologies close to the surface. The mixing of these different clasts in a near-surface environment without solar wind access is unusual.

The most straightforward explanation is that the breccia of Elmsborn represents a reaccreted rock after a

catastrophic collision between H and H/L chondrite parent bodies, complete disruption, and reassembly. This is the only conceivable way to prevent the implantation of solar wind gases in this kind of complex breccia, implying that the mixed components reassembled in some depth of the newly formed (at least) second generation parent body that was lithified like other breccia on planetary bodies by later impact processes, as described by Kieffer (1975) and Bischoff et al. (1983). A similar process could have resulted in the lack of solar wind in samples of Asteroid 2008TC<sub>3</sub> from the Almahata Sitta strewn field, a breccia containing even more diverse materials, though here a loss of fragile matrix between the various lithologies has been suggested (Bischoff, Bannemann, et al., 2022; Goodrich et al., 2019). Considering the process of late addition of diverse components by small impacts into the surface layers of a large first-generation OC parent body, it appears unrealistic that all the described fragmental components were added to the surface materials without including at least traces of solar wind gases.

#### Alternative Possibilities Concerning the Formation Process

We should at least mention and briefly discuss (and/or exclude) more exotic processes in order to understand the lack of a solar wind signature in the bulk breccia of Elmsborn: (a) It is highly unlikely that during the disruption and reassembly processes a fine-grained matrix that included all solar wind signatures on the precursor planetesimals was lost. All clasts in Elmsborn

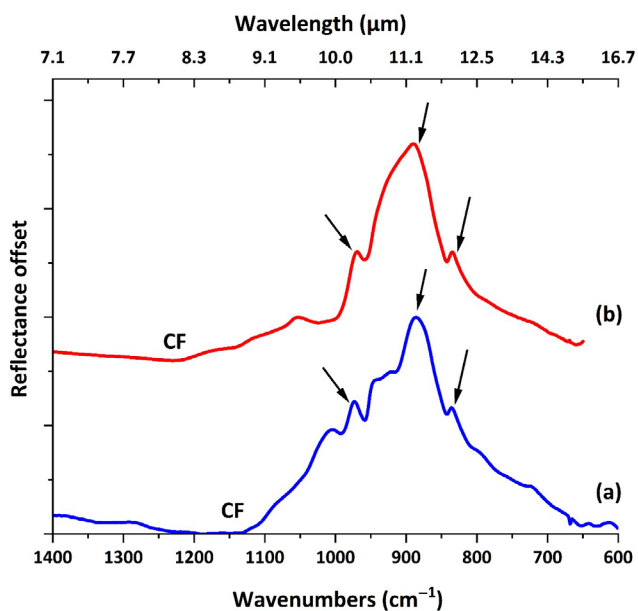


FIGURE 17. A micro-FT-IR spot measurement of the dark lithology of the Chelyabinsk meteorite (spectrum b) is compared to a spot measurement of a portion ( $200 \times 200 \mu\text{m}$ ) of the dark lithology of Elmshorn (spectrum a). Arrows denote typical olivine-related RB locations common in both spectra. However, Elmshorn displays additional RBs between  $947$  and  $917 \text{ cm}^{-1}$  owing to the presence of low-Ca pyroxene. The CF is shifted toward shorter wavenumbers ( $1140 \text{ cm}^{-1}$ ) when compared to the Chelyabinsk spectrum ( $1221 \text{ cm}^{-1}$ ).

seem compacted early and tightly and show no evidence for a once present additional fine-grained component. (b) Shielding from solar wind could be imaginable, but this would either require a very early process, within the first perhaps  $\sim 5$  Myr of the solar system, when the nebula gas was still present, or an extremely large parent body which could have once maintained a protective atmosphere. (c) Finally, it appears also unlikely that a very fast occurring regolithic process prevented the accumulation of detectable solar wind during formation of the breccia or that the residence time in a regolith was too short.

### Significance of Spectroscopic Research

All three studied lithologies from Elmshorn show a dominantly crystalline spectrum in the investigated areas (arrows in Figure 17 point at prominent Reststrahlen bands). The dark fine-grained and the light coarse-grained lithology (Figure 4) both display olivine-dominated spectra (Hofmeister, 1987). However, the olivine-rich groundmass that constitutes the dark fine-grained portion of the clast is adorned with additional peaks that are inconsistent with olivine and might point at the presence of “albitic” feldspars (see inset spectrum in Figure 17 for comparison), whereas the presence of chromite or

phosphate minerals, which were optically identified in the clast (Figure 7c), cannot be spectrally resolved. The light multiclastic main lithology appears to be dominated by a low-Ca pyroxene and shows additional RBs that point at the presence of additional silicate minerals that cannot be unambiguously identified: however, they are likely albitic feldspars (see inset red spectrum in Figure 17 for comparison). Neither metal nor sulfides can be resolved by diagnostic RBs in this measurement setup owing to the materials’ extremely low spectral contrast in this spectral range: instead, their presence is indirectly shown in an overall increased intensity (e.g., metals in Stojic et al., 2021). Prominent water bands were not detected in the spectra, indicating a continuous processing of the rock under dry conditions. A comparison with the shock-darkened lithology of the Chelyabinsk meteorite (Figure 9; Kohout et al., 2020; Morlok et al., 2017) shows that the most prominent RB of olivine is located at  $885 \text{ cm}^{-1}$  ( $11.3 \mu\text{m}$ ), which is common for both spectra. However, additional peaks belonging to low-Ca pyroxene in the dark portion of the Elmshorn meteorite might be indicative of a lesser shock degree than that of Chelyabinsk, which is of shock stage S4.

### Complex Breccias and the Mixing of OC Clasts

Inspecting the broken surfaces and the polished thin sections of Elmshorn (Figure 4) showed, as did the results of physical properties (density, MS) and of randomly obtained olivine compositions (Figure 8), that the rock is a complex breccia, indicating the presence of an impact-produced mixture of H and H/L (or L) chondrite lithologies and other types of clasts (e.g., Figures 5, 7, 9, and Figures S4–S6). In comparison, Kaidun and Almahata Sitta are probably the most spectacular breccias with a huge and even much wider variety of xenolithic clasts (e.g., Bischoff et al., 2010; Bischoff, Bannemann, et al., 2022; Goodrich et al., 2014; Goodrich et al., 2019; Horstmann et al., 2010; Horstmann & Bischoff, 2014; Ivanov, 1989; Zolensky & Ivanov, 2003; Zolensky et al., 1996, 2010). Also, some OC breccias have a huge variety of parent body lithologies as well as xenoliths, of which Adzhi-Bogdo (stone) and NWA 869 are excellent examples (Bischoff et al., 1993; Metzler et al., 2010, 2011; Welten et al., 2011). The Adzhi-Bogdo (LL3-6) chondrite regolith breccia contains fragmental breccia clasts, shock-darkened fragments, highly recrystallized clasts (sometimes with internal shock veins), melt rock clasts, and xenolithic L chondrite and achondritic clasts including granite-like lithologies (Bischoff et al., 1993, 1996; Terada & Bischoff, 2009). Similarly, NWA 869 contains unequilibrated and equilibrated chondrite clasts, impact melt rocks, an unequilibrated microbreccia, and several other objects (Metzler et al., 2011). Xenolithic fragments

have also been encountered in some accretionary type 3 breccias and other chondrite breccias: examples are Glanerbrug (Niemeier & Bischoff, 2006; Welten et al., 1992) and Villalbeto de la Pena (Bischoff et al., 2013; Dyl et al., 2012). Villalbeto de la Pena is an L6 breccia with a winonaite-related clast, while Glanerbrug is a very complex fragmental breccia representing a mixture of L and LL chondrite components, with the host rock being of LL chondritic origin (Niemeier & Bischoff, 2006; Welten et al., 1992). Similarly, Gattacceca et al. (2017) describe the brecciated LL6 chondrite Northwest Africa (NWA) 5764 that contains a  $>16\text{ cm}^3$  L4 clast. However, in general, mixing of clasts from different OC groups is relatively rare: In the LL chondrite St. Mesmin, intensely shocked H-group chondrite fragments were found (Dodd, 1974), and Rubin et al. (1983) described an LL5 clast in the Dimmitt H chondrite regolith breccia. Some other reports of identifying foreign OC clasts in meteoritic breccias have been made by Lipschutz et al. (c) based on chemical, mineralogical, and/or oxygen isotope characteristics. The detection of H chondrite clasts in the Roosevelt Co. (L5) chondrite has been described based on chemical and mineralogical data as well as on oxygen isotope characteristics (Lipschutz et al., 1983). Thus, the discovery of a few H chondrite clasts in L chondrite hosts has rarely been observed, but the roughly 50:50 mixing of H- and H/L- (or L-) group-like components in Elmsborn as mainly indicated by the results on the MS (Figure 16) has, to our knowledge, never been observed.

### The Elmsborn Meteorite and the Fall Statistics in Central Europe

In the last 10 years, 11 meteorite falls have been recovered in an area with less than a 500-km radius. Ten falls were OCs, while Flensburg represents a small extraordinary C1 chondrite of only 24 g (Bischoff et al., 2021). Considering the other meteorite falls of Braunschweig (L6: Bartoschewitz et al., 2017), Hradec Králové (LL5: 2016: The Meteoritical Bulletin), Broek in Waterland (L6, 2017: The Meteoritical Bulletin), Žďár nad Sázavou (L3: Spurný, 2016; Spurný et al., 2016), Ejby (H5/6: Haack et al., 2019; Spurný et al., 2017), Stubenberg (LL6: Bischoff et al., 2017; Ebert & Bischoff, 2016b; Spurný et al., 2016), Renchen (L5-6: Bischoff, Barrat, et al., 2019), Kindberg (L6, 2020: The Meteoritical Bulletin), and Antonin (Bischoff, Patzek, et al., 2022; Shrubeny et al., 2022), Elmsborn is the 10th recovered OC fall since 2013. Thus, it is obvious that the number of meteorite falls in Central Europe is remarkable, and it is certainly (at least in part) related to the successful work of the European Fireball Network and the excellent initiatives of the American Meteor Society (AMS:

<https://www.amsmeteors.org/>) and the International Meteor Organization (IMO: <https://fma.imo.net>).

### Conclusions

Elmsborn is the 11th recovered meteorite fall in the last 10 years in Central Europe within an area having a radius less than 500 km and the 10th OC (the other fall, Flensburg, is a small extraordinary C1 chondrite).

In total, 21 stones with a mass of 4277 g were recovered within a strewn field of about  $1.5 \times 2.5\text{ km}^2$  (Figure 2). The presence of short-lived cosmogenic radionuclides with half-lives as short as 5.6 days (Table 11) proves that the Elmsborn meteorite was recently exposed to cosmic rays in space.

Considering the densities of the individual stones, two samples were found to have densities of about  $3.34 \pm 0.01\text{ g cm}^{-3}$ , while the third one was found to have a significantly higher density of  $3.45 \pm 0.01\text{ g cm}^{-3}$ : these values are similar to those of L and H chondrites, respectively. The MS is highly variable between different stones, which suggests that the Elmsborn individuals consist of a mixture of H and L chondrite-like components.

Inspection of the broken surfaces and the polished thin sections revealed the brecciated texture of Elmsborn (Figure 4). Randomly obtained olivine compositions indicate the presence of an impact-produced mixture of H and H/L (or L) chondrite lithologies (Figure 8). Fragments include H6 chondrite clasts from the interior of a parent body as well as near-surface materials (clasts of types 3 and 4) mixed together with shock-darkened fragments and various clasts of different types of (impact) melts (e.g., Figures 5 and 9).

Because the samples, which show L chondrite characteristics based on physical properties (density, MS: Table 12 and Table S3), have O isotopic compositions of H chondrites (Figure 10), Elmsborn is classified as an anomalous H chondrite breccia. In line with this, the nucleosynthetic Ti and Cr isotope data places Elmsborn with OCs. Consequently, equilibrated, type 4 lithologies with mean olivine compositions of  $\text{Fa}_{21-23}$  obviously belong to the H group chondrite components.

The breccia does not contain solar wind-implanted noble gases, indicating that its different components cannot have been part of a parent body regolith. The gas retention ages of about 2.8 Gyr possibly indicate the closure time after the catastrophic collision between H and H/L (or L) chondrite parent bodies, while the CRE age for Elmsborn, which had a preatmospheric radius of 25–40 cm, is  $\sim 17\text{--}20\text{ Myr}$ .

In such a case of a complex polymict fragmental breccia the use of physical properties alone, like MS and



density, is not sufficient to allow an **unambiguous assignment** between H and L chondrites.

**Acknowledgments**—One of the studied samples was donated by Michael and Vanessa Pöhlmann, and we greatly acknowledge this wonderful support. We further thank Stephanie Adler, Ulla Heitmann, Maik Trogisch, Dennis Kohl, Oliver Sachs, Siegfried Haberer, Carsten Jonas, Oliver Lenzen, Lukasz Smula, Magda Skirzewska, Peter Steier, and Carlos Vivo-Vilches for technical, analytical, and photographic assistance and help as well as Celeste Brennecke for editorial support. We acknowledge the helpful reviews of Alan Rubin and Josep Trigo-Rodriguez and thank the Associate Editor Mike Zolensky. Discussion with Ingo Leya on production rates is highly appreciated. We also acknowledge the help of members of Fa. Digimold Reverse Engineering (96515 Sonneberg, Germany), who digitalized the largest sample and Emil Azar of the company 3D-MT in Augsburg (Germany). This work is partly funded by the Deutsche Forschungsgemeinschaft (DFG, German Research Foundation)—Project-ID 263649064—TRR 170 and TRR 170 Publication No. 214. M.P. is funded by a Sofja Kovalevskaja Award of the Alexander von Humboldt Foundation. This work (R.M.L.A., H.B., M.E., M.R., M.S.) has partially been carried out within the framework of the NCCR PlanetS supported by the Swiss National Science Foundation under grant 51NF40\_205606. Open Access funding enabled and organized by Projekt DEAL.

**Data Availability Statement**—Data available on request from the authors.

**Editorial Handling**—Dr. Michael Zolensky

## REFERENCES

- Alaerts, L., Lewis, R. S., and Anders, E. 1979. Isotopic Anomalies of Noble Gases in Meteorites and their Origins—III. LL-Chondrites. *Geochimica et Cosmochimica Acta* 43: 1399–1415.
- Alexander, C. M. O'D. 2019. Quantitative Models for the Elemental and Isotopic Fractionations in the Chondrites: The Non-carbonaceous Chondrites. *Geochimica et Cosmochimica Acta* 254: 246–276.
- Alexeev, V., Gorin, V., Ivliev, A., Kashkarov, L., and Ustinova, G. 2001. Combined Study of Thermoluminescence, Tracks, and Radionuclides in the Recently Fallen Kunya-Urgench Chondrite. *Geochemistry International* 39: 1043–55.
- Alexeev, V. A. 2003. Meteorite Ablation Evaluated from Data on the Distribution of Cosmogenic Neon Isotopes. *Solar System Research* 37: 207–217.
- Barrat, J.-A., Gillet, P., Dauphas, N., Bollinger, C., Etoubleau, J., Bischoff, A., and Yamaguchi, A. 2016. Evidence from Tm Anomalies for Non-CI Refractory Lithophile Element Proportions in Terrestrial Planets and Achondrites. *Geochimica et Cosmochimica Acta* 176: 1–17.
- Barrat, J.-A., Zanda, B., Moynier, F., Bollinger, C., Liorzou, C., and Bayron, G. 2012. Geochemistry of CI Chondrites: Major and Trace Elements, and Cu and Zn Isotopes. *Geochimica et Cosmochimica Acta* 83: 79–92.
- Bartoschewitz, R., Appel, P., Barrat, J.-A., Bischoff, A., Caffee, M. W., Franchi, I. A., Gabelica, Z., et al. 2017. The Braunschweig Meteorite—A Recent L6 Chondrite Fall in Germany. *Chemie der Erde—Geochemistry* 77: 207–224.
- Basford, J. R., Dragon, J. C., Pepin, R. O., Coscio, M. R., Jr., and Murthy, V. R. 1973. Krypton and Xenon in Lunar Fines. *4th Lunar and Planetary Science Conference*, pp. 1915–1955.
- Bischoff, A., Alexander, C. M. O'D., Barrat, J.-A., Burkhardt, C., Busemann, H., Degering, D., Di Rocco, T., et al. 2021. The Old, Unique CI Chondrite Flensburg—Insight into the First Processes of Aqueous Alteration, Brecciation, and the Diversity of Water-Bearing Parent Bodies and Lithologies. *Geochimica et Cosmochimica Acta* 293: 142–186.
- Bischoff, A., Bannemann, L., Decker, S., Ebert, S., Haberer, S., Heitmann, U., Horstmann, M., et al. 2022. Asteroid 2008 TC<sub>3</sub>, Not a Polymict Ureilitic but a Polymict CI Chondrite Parent Body? Survey of 249 Almahata Sitta Fragments. *Meteoritics & Planetary Science* 57: 1339–64.
- Bischoff, A., Barrat, J.-A., Bauer, K., Burkhardt, C., Busemann, H., Ebert, S., Gonsior, M., et al. 2017. The Stubenberg Meteorite - an LL6 Chondrite Fragmental Breccia Recovered Soon after Precise Prediction of the Strewn Field. *Meteoritics & Planetary Science* 52: 1683–1703.
- Bischoff, A., Barrat, J.-A., Berndt, J., Borovicka, J., Burkhardt, C., Busemann, H., Hakenmüller, J., et al. 2019. The Renchen L5-6 Chondrite Breccia—The First Confirmed Meteorite Fall from Baden-Württemberg (Germany). *Geochemistry—Chemie der Erde* 79: 125525.
- Bischoff, A., Dyl, K. A., Horstmann, M., Ziegler, K., Wimmer, K., and Young, E. D. 2013. Reclassification of Villalbeto de la Peña—Occurrence of a Winonaite-Related Fragment in a Hydrothermally Metamorphosed Polymict L-Chondritic Breccias. *Meteoritics & Planetary Science* 48: 628–640.
- Bischoff, A., Geiger, T., Palme, H., Spettel, B., Schultz, L., Scherer, P., Schlüter, J., and Lkhamsuren, J. 1993. Mineralogy, Chemistry, and Noble Gas Contents of Adzhi-Bogdo—An LL3-6 Chondritic Breccia with L-Chondritic and Granitoidal Clasts. *Meteoritics* 28: 570–78.
- Bischoff, A., Gerel, O., Buchwald, V. F., Spettel, B., Loeken, T., Schultz, L., Weber, H. W., et al. 1996. Meteorites from Mongolia. *Geochimica et Cosmochimica Acta* 31: 152–57.
- Bischoff, A., Horstmann, M., Pack, A., Laubenstein, M., and Haberer, S. 2010. Asteroid 2008 TC<sub>3</sub>—Almahata Sitta: A Spectacular Breccia Containing Many Different Ureilitic and Chondritic Lithologies. *Meteoritics & Planetary Science* 45: 1638–56.
- Bischoff, A., and Keil, K. 1983a. Ca-Al-Rich Chondrules and Inclusions in Ordinary Chondrites. *Nature* 303: 588–592.
- Bischoff, A., and Keil, K. 1983b. Catalog of Al-Rich Chondrules, Inclusions and Fragments in Ordinary Chondrites. Special Publication No. 22, UNM, Institute of Meteoritics, Albuquerque, 1–33.
- Bischoff, A., and Keil, K. 1984. Al-Rich Objects in Ordinary Chondrites: Related Origin of Carbonaceous and

- Ordinary Chondrites and their Constituents. *Geochimica et Cosmochimica Acta* 48: 693–709.
- Bischoff, A., Patzek, M., Di Rocco, T., Pack, A., Stojic, A., Berndt, J., and Peters, S. 2023. Saint-Pierre-le-Viger (L5-6) from Asteroid 2023 CX<sub>1</sub> Recovered in the Normandy, France—220 Years after the Historic Fall of L'Aigle (L6 Breccia) in the Neighborhood. *Meteoritics & Planetary Science* 58: 1385–98.
- Bischoff, A., Patzek, M., Peters, S. T. M., Barrat, J.-A., Di Rocco, T., Pack, A., Ebert, S., Jansen, C. A., and Kmiecik, K. 2022. The Chondrite Breccia of Antonin (L4-5)—A New Meteorite Fall from Poland with a Heterogeneous Distribution of Metal. *Meteoritics & Planetary Science* 57: 2127–42.
- Bischoff, A., Rubin, A. E., Keil, K., and Stöffler, D. 1983. Lithification of Gas-Rich Chondrite Regolith Breccias by Grain Boundary and Localized Shock Melting. *Earth and Planetary Science Letters* 66: 1–10.
- Bischoff, A., Schleiting, M., and Patzek, M. 2019. Shock Stage Distribution of 2280 Ordinary Chondrites—Can Bulk Chondrites with a Shock Stage S6 Exist as Individual Rocks? *Meteoritics & Planetary Science* 54: 2189–2202.
- Bischoff, A., Schleiting, M., Wieler, R., and Patzek, M. 2018. Brecciation among 2280 Ordinary Chondrites—Constraints on the Evolution of their Parent Bodies. *Geochimica et Cosmochimica Acta* 238: 516–541.
- Bischoff, A., Scott, E. R. D., Metzler, K., and Goodrich, C. A. 2006. Nature and Origins of Meteoritic Breccias. In *Meteorites and the Early Solar System II*, edited by D. S. Lauretta, and H. Y. McSween, Jr., 679–712. Tucson, Arizona: University of Arizona.
- Bischoff, A., and Stöffler, D. 1992. Shock Metamorphism as a Fundamental Process in the Evolution of Planetary Bodies: Information from Meteorites. *European Journal of Mineralogy* 4: 707–755.
- Bischoff, A., Storz, J., Barrat, J.-A., Heinlein, D., Jull, A. J. T., Merchel, S., Pack, A., and Rugel, G. 2022. Blaubeuren, Cloppenburg, and Machtenstein—Three Recently Recognized H-Group Chondrite Finds in Germany with Distinct Terrestrial Ages and Weathering Effects. *Meteoritics & Planetary Science* 57: 136–153.
- Burkhardt, C., Dauphas, N., Tang, H., Fischer-Gödde, M., Qin, L., Chen, J. H., Rout, S. S., Pack, A., Heck, P. H., and Papanastassiou, D. A. 2017. In Search of the Earth-Forming Reservoir: Mineralogical, Chemical and Isotopic Characterizations of the Ungrouped Achondrite NWA 5363/5400 and Selected Chondrites. *Meteoritics & Planetary Science* 52: 807–826.
- Busemann, H., Baur, H., and Wieler, R. 2000. Primordial Noble Gases in “Phase Q” in Carbonaceous and Ordinary Chondrites Studied by Closed-System Stepped Etching. *Meteoritics & Planetary Science* 35: 949–973.
- Clayton, R. N., Onuma, N., and Mayeda, T. K. 1976. A Classification of Meteorites Based on Oxygen Isotopes. *Earth and Planetary Science Letters* 30: 10–18.
- Consolmagno, G. J., Britt, D. T., and Macke, R. J. 2008. The Significance of Meteorite Density and Porosity. *Chemie der Erde* 68: 1–29.
- Dalcher, N., Caffee, M. W., Nishiizumi, K., Welten, K. C., Vogel, N., Wieler, R., and Leya, I. 2013. Calibration of Cosmogenic Noble Gas Production in Ordinary Chondrites Based on <sup>36</sup>Cl-<sup>36</sup>Ar Ages. Part 1: Refined Produced Rates for Cosmogenic <sup>21</sup>Ne and <sup>38</sup>Ar. *Meteoritics & Planetary Science* 48: 1841–62.
- Dodd, R. T. 1974. Petrology of the St. Mesmin Chondrite. *Contributions to Mineralogy and Petrology* 46: 129–145.
- Dos Santos, E., Gattacceca, J., Rochette, P., Fillion, G., and Scorzelli, R. B. 2015. Kinetics of Tetrataenite Disordering. *Journal of Magnetism and Magnetic Materials* 375: 234–241.
- Dyl, K. A., Bischoff, A., Ziegler, K., Young, E. D., Wimmer, K., and Bland, P. A. 2012. Early Solar System Hydrothermal Activity in Chondritic Asteroids on 1-10-Year Timescales. *Proceedings of the National Academy of Sciences of the USA* 109: 18306–11.
- Ebert, S., and Bischoff, A. 2016a. Genetic Relationship between Na-Rich Chondrules and Ca,Al-Rich Inclusions? Formation of Na-Rich Chondrules by Melting of Refractory and Volatile Precursors in the Solar Nebula. *Geochimica et Cosmochimica Acta* 177: 182–204.
- Ebert, S., and Bischoff, A. 2016b. The Stubenberg (Bavaria) Ordinary Chondrite Breccia: The Latest German Meteorite Fall. *Meteoritics & Planetary Science* 51: 6137.
- Gattacceca, J., Krzesinska, A. M., Marrocchi, Y., Meier, M. M., Bourot-Denise, M., and Lenssen, R. 2017. Young Asteroid Mixing Revealed in Ordinary Chondrites: The Case of NWA 5764, a Polymict LL Breccia with L Clasts. *Meteoritics & Planetary Science* 52: 2289–2304.
- Gattacceca, J., Suavet, C., Rochette, P., Weiss, B. P., Winklhofer, M., Uehara, M., and Friedrich, J. 2014. Metal Phases in Ordinary Chondrites: Magnetic Hysteresis Properties and Implications for Thermal History. *Meteoritics & Planetary Science* 49: 652–676.
- Geppert, C., Müller, P., Wendt, K., Schnabel, C., Synal, H.-A., Herpers, U., and Merchel, S. 2005. Intercomparison Measurements between Accelerator and Laser-Based Mass Spectrometry for Ultra-Trace Determination of <sup>41</sup>Ca in the 10<sup>-11</sup> to 10<sup>-10</sup> Isotopic Range. *Nuclear Instruments and Methods in Physics Research Section B* 229: 519–526.
- Gerber, S., Burkhardt, C., Budde, G., Metzler, K., and Kleine, T. 2017. Mixing and Transport of Dust in the Early Solar Nebula as Inferred from Titanium Isotope Variations among Chondrules. *Astrophys. J.* 841: L17.
- Goodrich, C. A., Bischoff, A., and O'Brien, D. P. 2014. Asteroid 2008 TC<sub>3</sub> and the Fall of Almahata Sitta, a Unique Meteorite Breccia. *Elements* 10: 31–37.
- Goodrich, C. A., Zolensky, M., Fioretti, A. M., Shaddad, M. H., Downes, H., Hiroi, T., et al. 2019. The First Samples from Almahata Sitta Showing Contacts between Ureilitic and Chondritic Lithologies: Implications for the Structure and Composition of Asteroid 2008 TC<sub>3</sub>. *Meteoritics & Planetary Science* 54: 2769–2813.
- Haack, H., Sørensen, A. N., Bischoff, A., Patzek, M., Barrat, J.-A., Midtskoge, S., Stempel, E., et al. 2019. Ejby—A New H5/6 Ordinary Chondrite Fall in Copenhagen, Denmark. *Meteoritics & Planetary Science* 54: 1853–69.
- Herwartz, D., Pack, A., Friedrichs, B., and Bischoff, A. 2014. Identification of the Giant Impactor Theia in Lunar Rocks. *Science* 344: 1146–50.
- Hofmeister, A. M. 1987. Single-Crystal Absorption and Reflection Infrared Spectroscopy of Forsterite and Fayalite. *Physics and Chemistry of Minerals* 14: 499–513.
- Horstmann, M., and Bischoff, A. 2014. The Almahata Sitta Polymict Breccia and the Late Accretion of Asteroid 2008 TC<sub>3</sub>—Invited Review. *Chemie der Erde—Geochemistry* 74: 149–184.
- Horstmann, M., Bischoff, A., Pack, A., and Laubenstein, M. 2010. Almahata Sitta—Fragment MS-CH: Characterization

- of a New Chondrite Type. *Meteoritics & Planetary Science* 45: 1657–67.
- DDEP. 2023. DDEP (Decay Data Evaluation Project) website <http://www.nucleide.org/Laraweb/index.php>.
- The Meteoritical Bulletin, 2023. <https://www.lpi.usra.edu/meteor/about.php>
- Huss, G. R., and Lewis, R. S. 1994. Noble Gases in Presolar Diamonds I: Three Distinct Components and their Implications for Diamond Origins. *Meteoritics* 29: 791–99.
- Ivanov, A. V. 1989. The Kaidun Meteorite: Composition and History. *Geochemistry International* 26: 84–91.
- Jörg, G., Amelin, Y., Kossert, K., Lierse, V., and Gostomski, C. 2012. Precise and Direct Determination of the Half-Life of  $^{41}\text{Ca}$ . *Geochimica et Cosmochimica Acta* 88: 51–65.
- Keil, K. 1982. Composition and Origin of Chondritic Breccias. In *Workshop on Lunar Breccias and Soils and their Meteoritic Analogs*, edited by G. J. Taylor, and L. L. Wilkening, 65–83. LPI Technical Report 82-02. Houston: Lunar Planetary Institute.
- Kieffer, S. W. 1975. From Regolith to Rock by Shock. *The Moon* 13: 301–320.
- Kohout, T., Haloda, J., Halodová, P., Meier, M. M. M., Maden, C., Busemann, H., Laubenstein, M., et al. 2017. Annama H Chondrite—Mineralogy, Physical Properties, Cosmic Ray Exposure, and Parent Body History. *Meteoritics & Planetary Science* 52: 1525–41.
- Kohout, T., Petrova, E. V., Yakovlev, G. A., Grokhovsky, V. I., Penttilä, A., Maturilli, A., Moreau, J.-G., et al. 2020. Experimental Constraints on the Ordinary Chondrite Shock Darkening Caused by Asteroid Collisions. *Astronomy & Astrophysics* 639: A146.
- Lachner, J., Martschini, M., Kalb, A., Kern, M., Marchhart, O., Plasser, F., Priller, A., Steier, P., Wieser, A., and Golser, R. 2021. Highly Sensitive  $^{26}\text{Al}$  Measurements by Ion-Laser-InterAction Mass Spectrometry. *International Journal of Mass Spectrometry* 465: 116576.
- Leya, I., Hirtz, J., and David, J.-C. 2021. Galactic Cosmic Rays, Cosmic-Ray Variations, and Cosmogenic Nuclides in Meteorites. *The Astrophysical Journal* 910: 136.
- Leya, I., and Masarik, J. 2009. Cosmogenic Nuclides in Stony Meteorites Revisited. *Meteoritics & Planetary Science* 44: 1061–86.
- Lipschutz, M. E., Gaffey, M. J., and Pellas, P. 1989. Meteoritic Parent Bodies: Nature, Number, Size, and Relation to Present-Day Asteroids. In *Asteroids*, edited by R. P. Binzel, T. Gehrels, and M. S. Matthews, 740–777. Tucson, AZ: University Arizona Press.
- Lodders, K., and Fegley, B., Jr. 1998. *The Planetary Scientist's Companion*. New York: Oxford University Press. 371.
- Ludwig, F., Wagner, L., Al-Abdullah, T., Barnaföldi, G. G., Bemmerer, D., Degering, D., Schmidt, K., Suranyi, G., Szücs, T., and Zuber, K. 2019. The Muon Intensity in the Felsenkeller Shallow Underground Laboratory. *Astroparticle Physics* 112: 24–34.
- Martschini, M., Lachner, J., Hain, K., Kern, M., Marchhart, O., Pitters, J., Priller, A., et al. 2022. 5 Years of Ion-Laser Interaction Mass Spectrometry—Status and Prospects of Isobar Suppression in AMS by Lasers. *Radiocarbon* 64: 555–568.
- Mertens, C. A. K., Riebe, M. E. I., and Busemann, H. 2021. Probability of Cosmogenic Nuclide Production Rates. *52nd Lunar and Planetary Science Conference*, abstract #2098.
- Metzler, K., Bischoff, A., Greenwood, R. C., Palme, H., Gellissen, M., Hopp, J., Franchi, I. A., and Trieloff, M. 2011. The L3-6 Chondritic Regolith Breccia Northwest Africa (NWA) 869: (I) Petrology, Chemistry, Oxygen Isotopes, and Ar-Ar Age Determinations. *Meteoritics & Planetary Science* 46: 652–680.
- Metzler, K., Bischoff, A., Palme, H., and Gellissen, M. 2010. Impact Melt Rocks from the L3-6 Chondritic Regolith Breccia Northwest Africa (NWA) 869. *Meteoritics & Planetary Science* 45: A137.
- Moniot, R. K. 1980. Noble-Gas-Rich Separates from Ordinary Chondrites. *Geochimica et Cosmochimica Acta* 44: 253–271.
- Morlok, A., Bischoff, A., Patzek, M., Sohn, M., and Hiesinger, H. 2017. Chelyabinsk—A Rock with Many Different (Stony) Faces: An Infrared Study. *Icarus* 284: 431–442.
- Neumaier, S., Wojcik, M., Dombrowski, H., and Arnold, D. 2009. Improvements of a Low-Level Gamma-Ray Spectrometry System at the Underground Laboratory “UDO”. *Applied Radiation and Isotopes* 67: 726–730.
- Niederer, F. R., Papanastassiou, D. A., and Wasserburg, G. J. 1985. Absolute Isotopic Abundances of Ti in Meteorites. *Geochimica et Cosmochimica Acta* 49: 835–851.
- Niemeier, M., and Bischoff, A. 2006. Glanerbrug—An LL4-6 Fragmental Breccia with Huge L Chondritic Clasts. *37th Lunar and Planetary Science*, abstract #1625.
- Nier, A. O. 1950. A Redetermination of the Relative Abundances of the Isotopes of Carbon, Nitrogen, Oxygen, Argon and Potassium. *Physics Review* 77: 789–793.
- Niese, S., Köhler, M., and Gleisberg, B. 1998. Low-Level Counting Techniques in the Underground Laboratory “Felsenkeller” in Dresden. *Journal of Radioanalytical and Nuclear Chemistry* 233: 167–172.
- Nishiizumi, K., Regnier, S., and Marti, K. 1980. Cosmic Ray Exposure Ages of Chondrites, Pre-Irradiation and Constancy of Cosmic Ray Flux in the Past. *Earth and Planetary Science Letters* 50: 156–170.
- Norris, T. L., Gancarz, A. J., Rokop, D. J., and Thomas, K. W. 1983. Half-Life of  $^{26}\text{Al}$ . *Journal of Geophysical Research Supplement* 8: B331–B333.
- Pack, A., and Herwartz, D. 2014. The Triple Oxygen Isotope Composition of the Earth Mantle and Understanding  $\Delta^{17}\text{O}$  Variations in Terrestrial Rocks and Minerals. *Earth and Planetary Science Letters* 390: 138–145.
- Pack, A., Höweling, A., Hezel, D. C., Stefanak, M., Beck, A. K., Peters, S. T. M., Sengupta, S., Herwartz, D., and Folco, L. 2017. Tracing the Oxygen Isotope Composition of the Upper Earth Atmosphere Using Cosmic Spherules. *Nature Communications* 8: 15702.
- Pack, A., Tanaka, R., Hering, M., Sengupta, S., Peters, S., and Nakamura, E. 2016. The Oxygen Isotope Composition of San Carlos Olivine on VSMOW2-SLAP2 Scale. *Rapid Communications in Mass Spectrometry* 30: 1495–1504.
- Paul, M., Ahmad, I., and Kutschera, W. 1991. Half-Life of  $^{41}\text{Ca}$ . *Zeitschrift für Physik A Hadrons and Nuclei* 340: 249–254.
- Peters, S. T. M., Alibabae, N., Pack, A., McKibbin, S. J., Raeisi, D., Nayebi, N., Torab, F., Ireland, T., and Lehmann, B. 2020. Triple Oxygen Isotope Variations in Magnetite from Iron-Oxide Deposits, Central Iran, Record Magmatic Fluid Interaction with Evaporite and Carbonate Host Rocks. *Geology* 48: 211–15.

- Peters, S. T. M., Fischer, M. B., Pack, A., Szilas, K., Appel, P. W. U., Muenker, C., Dallai, L., and Marien, C. S. 2021. Tight Bounds on Missing Late Veneer in Early Archean Peridotite from Triple Oxygen Isotopes. *Geochemical Perspectives Letters* 18: 27–31.
- Riebe, M. E. I., Welten, K. C., Meier, M. M. M., Wieler, R., Barth, M. I. F., Ward, D., Laubenstein, M., et al. 2017. Cosmic-Ray Exposure Ages of Six Chondritic Almahata Sitta Fragments. *Meteoritics & Planetary Science* 52: 2353–74.
- Rochette, P., Sagnotti, L., Bourot-Denise, M., Consolmagno, G., Folco, L., Gattacceca, J., Osete, M. L., and Pesonen, L. 2003. Magnetic Classification of Stony Meteorites: 1 Ordinary Chondrites. *Meteoritics & Planetary Science* 38: 251–58.
- Rubin, A. E. 1990. Kamacite and Olivine in Ordinary Chondrites: Intergroup and Intragroup Relationships. *Geochimica et Cosmochimica Acta* 54: 1217–32.
- Rubin, A. E., Scott, E. R. D., Taylor, G. J., Keil, K., Allen, J. S. B., Mayeda, T. K., Clayton, R. N., and Bogard, D. D. 1983. Nature of the H Chondrite Parent Body Regolith: Evidence from the Dimmitt Breccia. *Journal of Geophysical Research* 88: A741–A754.
- Rubin, A. E., and Turrin, B. D. 2023. Nature and Timing of a Significant Reduction Event on the L-Chondrite Parent Asteroid. *Meteoritics & Planetary Science* 59: 836–857. <https://doi.org/10.1111/maps.14088>.
- Rüfenacht, M., Morino, P., Lai, Y.-J., Fehr, M. A., Haba, M. K., and Schönbächler, M. 2023. Genetic Relationships of Solar System Bodies Based on their Nucleosynthetic Ti Isotope Compositions and Sub-Structures of the Solar Protoplanetary Disk. *Geochimica et Cosmochimica Acta* 355: 110–125.
- Rugel, G., Pavetich, S., Akhmadaliev, S., Enamorado Baez, S. M., Scharf, A., Ziegenrucker, R., and Merchel, S. 2016. The First Four Years of the AMS-Facility DREAMS: Status and Developments for more Accurate Radionuclide Data. *Nuclear Instruments and Methods in Physics Research Section B* 370: 94–100.
- Sharp, Z. D., Gibbons, J. A., Atudorei, V., Pack, A., Sengupta, S., Shock, E. L., and Knauth, L. P. 2016. A Calibration of the Triple Oxygen Isotope Fractionation in the SiO<sub>2</sub>-H<sub>2</sub>O System and Applications to Natural Samples. *Geochimica et Cosmochimica Acta* 186: 105–119.
- Shields, W. R., Murphy, T. J., Catanzaro, E. J., and Garner, E. L. 1966. Absolute Isotopic Abundance Ratios and the Atomic Weight of a Reference Sample of Chromium. *Journal of Research of the National Institute of Standards and Technology* 70A: 193–97.
- Shrbeny, L., Krzesinska, A. M., Borovicka, J., Spurny, P., Tyminski, Z., and Kmiecik, K. 2022. Analysis of the Daylight Fireball of July 15, 2021, Leading to Meteorite Fall and Find near Antonin, Poland, and a Description of the Recovered Meteorite. *Meteoritics & Planetary Science* 57: 2108–26.
- Spurný, P. 2016. Instrumentally Documented Meteorite Falls: Two Recent Cases and Statistics from all Falls. In *Asteroids: New Observations, New Models*, edited by S. Chesley, A. Morbidelli, R. Jedicke, and D. Farnocchia, vol. 318, Proceedings IAU Symposium. Cambridge, UK: Cambridge University Press, pp. 69–79.
- Spurný, P., Borovička, J., Baumgarten, G., Haack, H., Heinlein, D., and Sørensen, A. N. 2017. Atmospheric Trajectory and Heliocentric Orbit of the Ejby Meteorite Fall in Denmark on February 6, 2016. *Planetary and Space Science* 143: 192–98.
- Spurný, P., Borovička, J., Haloda, J., Shrbený, L., and Heinlein, D. 2016. Two Very Precisely Instrumentally Documented Meteorite Falls: Žďár Nad Sázavou and Stubenberg—Prediction and Reality. *Meteoritics & Planetary Science* 51: A591.
- Steiger, R. H., and Jäger, E. 1977. Subcommittee on Geochronology: Convention on the Use of Decay Constants in Geo- and Cosmochronology. *Earth and Planetary Science Letters* 36: 359–362.
- Stöffler, D., Hamann, C., and Metzler, K. 2018. Shock Metamorphism of Planetary Silicate Rocks and Sediments: Proposal for an Updated Classification System. *Meteoritics & Planetary Science* 53: 5–49.
- Stöffler, D., Keil, D., and Scott, E. R. D. 1991. Shock Metamorphism of Ordinary Chondrites. *Geochimica et Cosmochimica Acta* 55: 3845–67.
- Stojic, A. N., Morlok, A., Tollan, P., Kohout, T., Hermann, J., Weber, I., Moreau, J.-G., et al. 2021. A Shock Recovery Experiment and its Implications for Mercury's Surface: The Effect of High Pressure on Porous Olivine Powder as a Regolith Analog. *Icarus* 357: 114162.
- Terada, K., and Bischoff, A. 2009. Asteroidal Granite-like Magmatism 4.53 Gyr ago. *The Astrophysical Journal* 699: L68–L71.
- Trinquier, A., Elliott, T., Ulfbeck, D., Coath, C., Krot, A. N., and Bizzarro, M. 2009. Origin of Nucleosynthetic Isotope Heterogeneity in the Solar Protoplanetary Disk. *Science* 324: 374–76.
- Ward, D., Bischoff, A., Roszjar, J., Berndt, J., and Whitehouse, M. J. 2017. Trace Element Inventory of Meteoritic Ca-Phosphates. *American Mineralogist* 102: 1856–80.
- Weber, I., Morlok, A., Grund, T., Bauch, K. E., Hiesinger, H., Stojic, A., Grumpe, A., et al. 2018. A Mid-Infrared Reflectance Database in Preparation for Space Missions. *48th Lunar and Planetary Science Conference*, abstract #1430.
- Welten, K., Leclerc, M. D., Ott, U., Metzler, K., Caffee, M. W., Jull, A. J. T., and Franke, L. 2011. The L3–6 Chondritic Regolith Breccia Northwest Africa (NWA) 869: (II) Noble Gases and Cosmogenic Radionuclides. *Meteoritics & Planetary Science* 46: 970–988.
- Welten, K. C., Lindner, L., Poorter, R. P. E., Kallemeyn, G. W., Rubin, A. E., and Wasson, J. T. 1992. The Glanerbrug Breccia: Evidence for a Separate L/LL Chondritic Parent Body? *Meteoritics* 27: A307.
- Wieler, R. 2002. Cosmic-Ray-Produced Noble Gases in Meteorites. *Reviews in Mineralogy and Geochemistry* 47: 125–170.
- Williams, N. H. 2015. The Origin of Titanium Isotopic Anomalies within Solar System Material PhD thesis, The University of Manchester.
- Williams, N. H., Fehr, M. A., Parkinson, I. J., Mandl, M. B., and Schönbächler, M. 2021. Titanium Isotope Fractionation in Solar System Materials. *Chemical Geology* 568: 120009.
- Wostbrock, J. A., Cano, E. J., and Sharp, Z. D. 2020. An Internally Consistent Triple Oxygen Isotope Calibration of Standards for Silicates, Carbonates and Air Relative to VSMOW2 and SLAP2. *Chemical Geology* 533: 119432.
- Zhang, J., Dauphas, N., Davis, A. M., Leya, I., and Fedkin, A. 2012. The Proto-Earth as a Significant Source of Lunar Material. *Nature Geoscience* 5: 251–55.
- Zhang, J., Dauphas, N., Davis, A. M., and Pourmand, A. 2011. A New Method for MC-ICPMS Measurement of

Titanium Isotopic Composition: Identification of Correlated Isotope Anomalies in Meteorites. *Journal of Analytical Atomic Spectrometry* 26: 2197–2205.

Zolensky, M., Herrin, J., Mikouchi, T., Ohsumi, K., Friedrich, J., Steele, A., Rumble, D., et al. 2010. Mineralogy and Petrography of the Almahata Sitta Ureilite. *Meteoritics & Planetary Science* 45: 1618–37.

Zolensky, M. E., and Ivanov, A. 2003. The Kaidun Microbreccia Meteorite: A Harvest from the Inner and Outer Asteroid Belt. *Chemie der Erde—Geochemistry* 63: 185–246.

Zolensky, M. E., Ivanov, A. V., Yang, S. V., Mittlefehldt, D. W., and Ohsumi, K. 1996. The Kaidun Meteorite: Mineralogy of an Unusual CM1 Lithology. *Meteoritics & Planetary Science* 31: 484–493.

## SUPPORTING INFORMATION

Additional supporting information may be found in the online version of this article.

**Table S1.** The Elmshorn finds (GPS coordinates of the locations referring to the WGS84 datum).

**Table S2.** Bulk compositional data for Elmshorn used here to determine the CRE ages and for Monte-Carlo production rate calculations for  $^{22}\text{Na}$  (Figure S7),  $^{26}\text{Al}$  and  $^{41}\text{Ca}$  (Figure 14); (1) Bulk chemistry measured with ICP-AES and ICP-SFMS (Table 5 in the manuscript); (2) average H chondrite composition taken from Alexander, 2019; (3) average H chondrite composition from Lodders and Fegley (1998); (4) calculated for the sum of all concentrations to reach 100 wt%.

**Table S3.** Magnetic susceptibility (in  $10^{-9} \text{ m}^3 \text{ kg}^{-1}$ ) of the majority of Elmshorn fragments (see Figure 16).

**Figure S1.** A CT slice of the specimen E02 (Table S1) of 233.5 g showing (a) sparse chondrules (dark gray), metal (white), and sulfide grains (light gray) as well as an elongated metal-sulfide intergrowth on the left side (arrow). (b) A large ( $\sim 5.5$  mm) nodule (arrow) consisting of sulfide and putatively chromite in the center of the sample. (c) A fragment with an intergrowth of silicates (dark gray, left edge), and an area with a high abundance of metal and sulfide (arrow). (d) Fragment with a significantly higher abundance of metal and sulfide in the top left.

**Figure S2.** A CT slice of a piece from the shattered E03 specimen of 51.62 g showing (a) millimeter-sized grains of metal and sulfide. (b) An area with a higher abundance of metal and sulfide at the top is indicated by the arrow. An elongated metal-sulfide association is noticeable. (c) Zoom-in from (b) illustrating the elongated metal-sulfide intergrowth. A  $\sim 3$  mm-sized porphyritic chondrule is also visible in the neighborhood (metal-free, dark area). (d) Potential shock-darkened fragment with Schlieren-like metal and sulfide.

**Figure S3.** Several CT scans of specimen E21 with a weight of 1.09 g.

**Figure S4.** (a) Fragment M from E03 is an unusual melt rock clast with skeletal (equilibrated) olivine ( $\text{Fa}_{26}$ ) embedded in a fine-grained groundmass (plane polarized light). (b) Fragment M in BSE image. (c) The porphyritic objects in a fine-grained groundmass consist of an intergrowth of two different phases (d), from which the darker one appears to be Ca pyroxene (BSE images).

**Figure S5.** The L3.9/4 chondrite fragments from E03 are difficult to identify and are indicated by the slightly lighter olivine grains compared with those of the surroundings.

**Figure S6.** Microscopic images from components in stone E07.

**Figure S7.** Specific  $^{22}\text{Na}$  activity measured in Elmshorn (red line with associated 1-sigma uncertainties) compared to radius- and depth-dependent (saturation) production rate for  $^{22}\text{Na}$  for L chondrites (Leya et al., 2021).